communications earth & environment

Article

A Nature Portfolio journal

https://doi.org/10.1038/s43247-026-03450-x

Permafrost thaw controls iron flux from wetlands and sulfide-bearing rocks to Arctic rivers and streams

Check for updates

Roman J. Dial [1,2] ✉, Caitlynn T. Hanna[3], Patrick F. Sullivan [2], David J. Cooper [4], Christopher J. Tino[5,6], Daniel D. Gregory[7], Charles Diamond[4], Michael Rieser [8], Dmitry J. Nicolsky [9], Kenneth Hill [10], Go Iwahana [11], Joshua C. Koch [12], Michael P. Carey [12], Lance Miller[13] & Timothy W. Lyons [4]

Recent warming has caused widespread iron mobilization into Arctic waterbodies that degrades ecosystems and threatens natural resources. Yet, understanding where and when iron flux occurs remains limited. Here, we investigate iron loading across regional to local scales in Arctic Alaska using climate, water chemistry, and borehole data together with mapped geology and permafrost presence. We show that both anoxic microbial iron reduction and acid rock drainage from iron-sulfide oxidation mobilize iron. Iron influx is strongly associated with lowland wetlands, sulfide-rich upland bedrock, and near-surface permafrost. Acid rock drainage chemistry correlates very strongly with the depth of seasonal thaw above permafrost from the previous year, indicating a one-year lag. These findings clarify the spatial and temporal dynamics of Arctic river rusting, provide a mechanistic understanding of the phenomenon, and may allow anticipation of its occurrence and assessment of its implications for aquatic ecosystem health and subsistence resources under ongoing climate change.

Rapid warming is fundamentally altering Earth system processes and so threatening ecosystem functioning worldwide[1]. One emerging threat—the widespread occurrence of metal precipitates discoloring formerly clear waterbodies in northern Canada[2], Alaska[3–5], Russia (Supplementary Fig. 1), and temperate[6–8] and tropical[9] mountains—is visibly dramatic. The leading hypothesis[2–9] for this phenomenon centers on warming-driven degradation of permafrost (ground that remains below 0 °C for at least two consecutive years) that deepens the seasonally thawed active layer and creates perennially unfrozen layers (taliks). New pathways in thawing permafrost allow liquid water and its dissolved constituents to interact with previously isolated substrates, mobilizing iron (Fe) and other metals from terrestrial sources to aquatic sinks[2–10].

Two main processes facilitate Fe mobilization as ferrous iron (Fe(II)) following thaw: oxidation of iron-sulfide minerals (e.g., pyrite, FeS_2, the most abundant iron-sulfide) as acid rock drainage (ARD)[2,4–11] and anaerobic microbial respiration as iron-reducing metabolism (FRM)[3–5,12–17]. In ARD[11], Fe(II) is initially liberated in acidic solution from bedrock through oxidation of iron-sulfides (such as FeS_2) by oxygen (O_2). Then, as the acidic solution is buffered in more neutral waters that are further exposed to O_2, the Fe(II) itself is subsequently oxidized and ultimately precipitated as rust-colored ferric iron (Fe(III)). In FRM[12,13], microbial reduction of Fe(III) under anoxic conditions produces Fe(II), which is then re-oxidized to Fe(III) when the anoxic solution is exposed to O_2. Notably, ARD produces acid (H^+) and sulfate (SO_4^{2-}) as reaction products[11], unlike FRM[12]. Definitive linkage between deepening active layer thickness (ALT) and ARD mobilization of Fe over multiple years—as shown previously for FRM[3]—is rare[7].

Rocks bearing iron-sulfide can also host other metal-sulfides[4–9] that release potentially toxic metals during ARD. These metals include among others zinc (Zn), lead (Pb), and copper (Cu). Low pH conditions also mobilize aluminum (Al) from surrounding rocks. Particulate Fe and Al are known to directly interfere with gill respiration in fish and other aquatic organisms[5,6]. Metal precipitates smother benthic communities and increase mortality of aquatic algae and invertebrates[4–7] that fish (such as juvenile salmon) consume. Metal mobilization can also degrade drinking water[18]

[1]Institute of Culture and Environment, Alaska Pacific University, Anchorage, AK, USA. [2]Environment and Natural Resources Institute, University of Alaska Anchorage, Anchorage, AK, USA. [3]Department of Civil Engineering, University of Alaska Fairbanks, Fairbanks, AK, USA. [4]Department of Forest and Rangeland Stewardship, Colorado State University, Fort Collins, CO, USA. [5]Department of Earth and Planetary Sciences, University of California, Riverside, CA, USA. [6]Department of Earth, Energy, and Environment, University of Calgary, Calgary, Canada. [7]Department of Earth Sciences, University of Toronto, Toronto, ON, Canada. [8]Teck Alaska Incorporated, Anchorage, AK, USA. [9]Geophysical Institute, University of Alaska Fairbanks, Fairbanks, AK, USA. [10]National Park Service, Arctic and Central Alaska Networks, Fairbanks, AK, USA. [11]University of Alaska Fairbanks, International Arctic Research Center, Fairbanks, AK, USA. [12]U.S. Geological Survey, Alaska Science Center, Anchorage, AK, USA. [13]NANA Regional Corporation, Anchorage, AK, USA. ✉e-mail: roman@alaskapacific.edu

and harm fisheries[5,19] used by human communities. Increase in sulfate of one major Alaskan river has been partially attributed to thaw-enhanced sulfide oxidation occurring in its Arctic tributaries[20]. Understanding where, when, and how river rusting occurs may assist in identifying additional factors causing salmon declines in northern Alaska[5,21].

During ARD, weathering of bedrock newly exposed to O_2 and containing metal-sulfides (e.g., FeS_2) initiates ARD. A simplified version is

$$2FeS_2 + 7O_2 + 2H_2O \rightarrow 2Fe(II) + 4SO_4^{2-} + 4H^+ \quad (1)$$

which continues until available FeS_2 is depleted[11] or hydrologic setting changes. Oxidation of sulfur to SO_4^{2-} is exothermic[11] and could further facilitate permafrost thaw[2,8] because of action by Fe- and sulfide-oxidizing bacteria adapted to cold environments[2]. Rust coloration from ARD occurs when Fe(II) in acidic solution is buffered and produces Fe(III) and Fe(III) (oxyhydr)oxide precipitates[8,11]. These complexes stain benthic sediments orange or remain suspended in the water column. Additional ARD products are acid and SO_4^{2-}. Dissolution of gypsum ($CaSO_4 \bullet H_2O$) also elevates SO_4^{2-} but does so in a molar ratio of SO_4^{2-}:Ca near one[20].

Anaerobic metabolism by microbes in saturated environments (like wetland soils) initiate FRM, mobilizing Fe(II) in anoxic solution[12,13]. In this process, heterotrophic microbes use Fe(III) as an electron acceptor during anaerobic respiration[12,13], producing Fe(II) as a byproduct[12–17]:

$$Fe(III) + \text{organic C} \rightarrow Fe(II) + CO_2 + H_2O \quad (2)$$

Rust coloration from FRM occurs when Fe(II) in anoxic groundwater is exposed to oxygen, producing Fe(III) and Fe(III)(oxyhydr)oxide precipitates[12,13]. Importantly, FRM can occur broadly in settings beyond iron-sulfide bearing bedrock, including wetland soils developed over alluvium and glacial till[3,14,15] (i.e., unconsolidated surficial deposits). While ARD is inherently acidic (pH < 4), the acidity of soils within wetlands that host FRM can range from pH < 5 in lowland black spruce forests and tussock sedge communities (where permafrost thaw enhances Al mobilization due to lower pH[2,8]) up to pH > 8 in riverine marshes and lakes[22]. Because FRM does not directly liberate SO_4^{2-}, high concentrations of Fe with little SO_4^{2-} suggest FRM.

After thaw, environmental conditions determine whether the Fe(II) produced by FRM is oxidized and precipitated as Fe(III)-bearing minerals within permafrost soils or is released into surface waters where it is oxidized and precipitated as Fe-(hydr)oxides[16,17]. In oxygenated conditions, lithotrophic microbes can oxidize Fe(II) back to Fe(III) before Fe(II) is flushed from wetland soils[12]. This Fe-cycling generates a dynamic equilibrium mediated by aerobic and anaerobic microbes[13]. However, Fe(II) may be lost faster than its reoxidation[16,17] during rapid expansion of anoxic environments, allowing its introduction to adjacent waterbodies.

Examples of FRM associated with ongoing deepening of active layers[3] or with active layers deeper relative to nearby habitats (space-for-time substitution studies[14–17]) have been documented in high-latitude wetlands. Extensive areas of high-latitude permafrost consist of poorly draining, carbon-rich, reducing soils[22]. Thus, FRM may become an increasingly important source of Fe (and atmospheric C) with continued permafrost thaw, and, importantly, is less directly controlled by local bedrock and specifically the metal sulfide minerals that drive ARD.

Given the complexities involved during permafrost thaw, we investigated river rusting in Arctic Alaska by considering rusting observations in the context of geology[23,24] and permafrost presence[25,26] at three spatial scales: regional, subregional, and local. Specifically, we sought to determine the roles of warming, geology, permafrost, and physical processes in determining the flux of iron into streams and rivers of Arctic Alaska from both wetlands and acid seeps.

At the regional scale (2.41×10^5 km^2), we focused on Alaska's Brooks Range[4] with its large-scale geology[23] and permafrost conditions[25]. At the subregional scale (2.02×10^3 km^2), we examined water samples collected in the basin of the Salmon River[5] within the roadless Kobuk Valley National Park (KOVA) and adjacent watersheds in the context of watershed lithology[24] and near-surface (<1 m) permafrost probability[26]. Water samples from six waterbody types (acid seeps, stained streams, clear streams, wetlands, the Salmon River and its mainstem, the Kobuk River) presented evidence that both ARD and FRM contribute Fe to surface waters. We explored the fate of Fe within the 100-km long Salmon River using Fe concentration and discharge estimates to calculate Fe flux in the mainstem and its tributaries. At the local scale (2.06×10^2 km^2), we analyzed water samples and ground temperatures in a landscape within the Ikalukrok Creek[27] watershed during a record warming period[28] (Fig. 1). There, Teck Alaska Incorporated (Anchorage, Alaska) drilled four boreholes within a single small catchment 11 km upstream of the Pb-Zn sulfide deposit Red Dog Mine (RDM). Borehole data from beneath two plant community types common across the Arctic biome (sedge meadow and low shrub tundra) were previously collected to calibrate an implementation of the Geophysical Institute Permafrost Laboratory model[29] (GIPL2) describing ground temperatures. Estimates of ALT from GIPL2 over 2015-2023 were then compared to ARD products measured downstream during the same period. Collectively, these datasets advance our understanding of where, how, and when Arctic river rusting occurs and provide insights that can be used in other Arctic systems[2–5,10,20,30–34] and periglacial settings[6–10,35] more generally.

Results

Annual thermal loss reached its minimum in 2019

Permafrost stability is maintained through heat loss from the ground. A sufficient reduction in annual ground heat loss destabilizes permafrost by substantially deepening ALT and forming taliks. Heat loss is calculated as

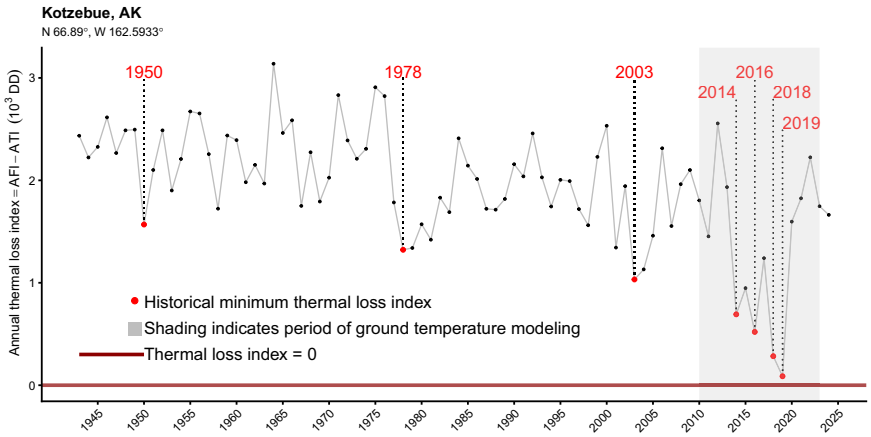

Fig. 1 | Declining permafrost stability at Kotzebue, Alaska, 1943–2023. Annual thermal loss index (AFI - ATI, where AFI and ATI are cumulative annual freezing-degree days and thawing-degree days) indicates net annual ground heat loss, with higher values representing greater permafrost stability. The 2010–2023 period (shaded) shows unprecedented instability, with thermal loss approaching zero in 2019 for the first time in 80 years. Labeled years indicate historical minima. Daily temperature from Kotzebue Ralph Wien Memorial Airport[59] (GHCND ID USW00026616).

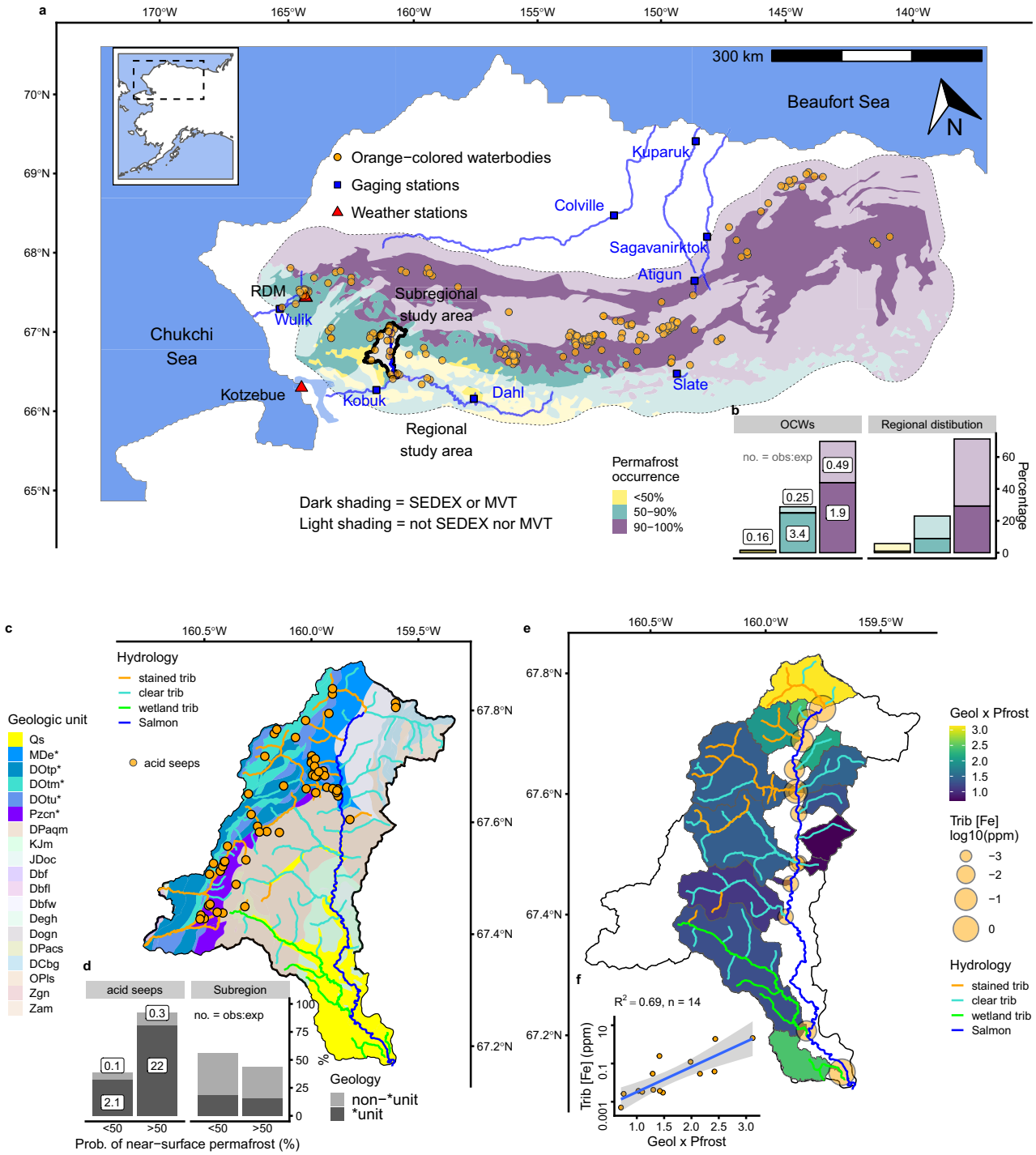

the balance between accumulated freezing (AFI) and thawing (ATI) air temperature indices[22,28] as absolute values that provide an annual thermal loss index (AFI − ATI). Continuous daily air temperatures recorded in Kotzebue from 1943 to 2023 indicate 2014–2019 was unprecedented in potential permafrost instability (Fig. 1) because the annual thermal loss index (mean = 1949 °C-days, $n = 80$ years) approached 0 °C-days for the first time over the 80-year record. Within the record's initial 61 years, minima in the annual thermal loss index occurred in 1950, 1978, and 2003 (mean = 1308 °C-days, $n = 3$ years). During 2014–2019, minima occurred in 2014, 2016, 2018, and 2019 which together averaged 396 °C-days.

Rusting is associated with lithology and permafrost

Regional rusting Among orange-colored waterbodies (OCWs) identified across the 1000 km-long Brooks Range (Fig. 2a), rusting was closely associated (Fig. 2b) with sedimentary and metasedimentary rocks of Paleozoic age hosting metal-sulfides derived from hydrothermal brines[23] in settings subject to discontinuous permafrost[25] (50% <permafrost occurrence ≤90%). Using observations from both field and recent remote sensing observations, we compared locations of the $n = 205$ OCWs to potential Zn-sulfide ore deposits (Zn-polygons) mapped by the U.S. Geological Survey[23] (USGS) and to modeled permafrost zonation[25]. The Zn-polygons represent deposits of hydrothermal origin that are generally hosted in pre-Mississippian (e.g.,

Fig. 2 | Regional and subregional study areas. a Regional study area enclosed by dotted line around Brooks Range of northern Alaska. Locations of orange-colored waterbodies (n = 205 OCWs, orange circles) identified in the field or with satellite imagery[4]. It is unknown how many may have been orange in the past, but of n = 82 OCWs from ref. 4 with two or more very-high (<3 m) resolution 2005–2022 satellite images (mean = 3.7 images per OCW), the mean annual percentage showing orange staining during 2003–2012 was 32% versus 74% during 2013–2022. Kotzebue and Red Dog Mine (RDM) weather stations (red triangles); discharge gaging stations (blue squares). Subregional study area (gray polygon) enclosing Kobuk Valley National Park (KOVA). Map made with Natural Earth. Free vector and raster map data @ naturalearthdata.com. **b** Percentage of OCWs and of region by permafrost and geology. In **a** and **b** permafrost occurrence[25] indicated as sporadic (<50% occurrence, yellow), discontinuous (50–100%, green), and continuous (90–100%, purple). Dark shading indicates potential Zn-ore bearing deposits (SEDEX and MVT)[23]. **c** Acid seeps (orange points), hydrology (lines), and geologic units[24] (polygons) in subregional study area. Blue line = Salmon River, light blue lines = clear tributaries, orange = stained tributaries, and green = tributaries draining primarily wetlands. Dark colored polygons indicate *units described in text and Quaternary surficial deposits. **d** Percentage of acid seeps (n = 62) and of subregion by geology (shading as *units vs. non *units) and probability of occurrence of near surface (<1 m) permafrost (<50 versus >50%). Numbers in boxes of **b** and **d** give odds ratios comparing seep odds to regional odds with comparable geologic and permafrost conditions. **e** Mapped visualization of variables used in linear regression model $Y = \beta_o + \beta_3 X_3 + \varepsilon$, where $Y = \log_{10}$(dissolved Fe), β_o = intercept, X_3= watershed geologic *unit and Qs area (Geol) multiplied by mean watershed probability of occurrence of near surface permafrost (Pfrost), β_3 = regression coefficient of X_3, and ε = normally distributed error as $N(0,\sigma)$. Point size indicates dissolved Fe concentration at mouth of 14 tributaries with pH >5. Lines indicate hydrology as in **c**. Polygons indicate tributary watersheds colored by X_3 value. **f** Scatterplot of Y vs. X_3 for the 14 tributaries in **c**, showing line of best fit with 95% confidence band, R^2, and sample size n. The dotted line in **a** is defined by a polygon enclosing named features on USGS 1:250,000 quadrangles that are identified as inside the Brooks Range by ref. 42 with an area calculated as 2.41×10^5 km² in a geographic information system (GIS). The outermost polygon boundary in **c** and **e** is defined by the watersheds of the Salmon River, Tukpahlearik Creek upstream of its confluence with Omar River, and Timber Creek upstream of 103 m above MSL with area calculated as 2.01×10^3 km² in a GIS.

Devonian) platform carbonates (MVT) or Mississippian to Pennsylvanian deep basin shales (SEDEX) and associated metasedimentary formations[23].

We quantified the association of OCWs with Zn-polygons and permafrost zonation by calculating the proportions of OCWs inside the combinations of Zn-polygons (i.e., inside and outside of Zn-polygons) with permafrost zones (continuous, discontinuous, and isolated/sporadic). We then compared the proportions of OCWs among the six combinations (two Zn-polygon settings x three permafrost zones) to the overall spatial proportions. The Zn-polygons within discontinuous permafrost covered 9% of the regional study area but hosted 25% of the OCWs. Thus, the odds of occurrence of OCWs within Zn-polygons subject to discontinuous permafrost were almost four times higher than expected from regional availability (odds ratio = 3.9). Forty-four percent of OCWs were located within Zn-polygons subject to continuous permafrost, with odds of OCW occurrence roughly twice those expected based on regional distribution of Zn-polygons in continuous permafrost (odds ratio = 1.9). Identified OCWs were much less likely to occur outside of Zn-polygons in continuous permafrost (odds ratio ≈ 0.25). OCWs were rare (<2%) in isolated or sporadic permafrost.

Subregional scale Acid seeps in the subregional area were associated with geologic units hosted within shale, schist, or marble of Mississippian to Devonian age subject to near-surface permafrost[26] along the continuous-discontinuous permafrost boundary[25] (Fig. 2c, d). We used field surveys and 1–3 m resolution imagery to locate ARD surfacing as seeps or springs where indicated by spatially abrupt changes in water color from clear to orange (n = 62 acid seeps = 38 imagery-located + 24 field-located). Soils overlying Mississippian-Devonian metasediments and metavolcanics[24] hosted most of these acid seeps (Supplementary Fig. 2a,c). Five units (here annotated as *units) contained 82% of seeps. Four *units (DOtp*, DOtm*, DOtu*, and MDe*) included pyritic schists or shales of ages that overlapped the Devonian (Supplementary Table 1). The fifth Paleozoic *unit (Pzcn*) interbedded marble with pyritic schist. The five *units plus three additional Devonian units (Dbfw, DPaqm, and DPacs) contained all 62 acid seeps. Acid seeps occurring in *units subject to near-surface permafrost probability[26] > 50% were 22 times more likely than random points subject to the same conditions (odds ratio = 22.0, Fig. 2d). In contrast, the odds of acid seeps in non-*units located with near-surface permafrost probability <50% were one-tenth the odds of the same condition among random points (odds ratio = 0.1).

Dissolved Fe in tributaries of the Salmon River (Fig. 2e) also showed a very strong association with both geologic units[24] and near-surface permafrost[26] (Fig. 2f). Using n = 14 Salmon River tributaries with pH >5 in August 2023, we modeled dissolved Fe through linear regression with predictor variables characterizing catchment-level lithology and permafrost. Our hypothesis testing used Y = log-transformed dissolved Fe as a linear function of three variables: within-catchment mean probability of near-surface (<1 m) permafrost[26] (*Near-surface permafrost probability*); log-transformed within-catchment area of four mapped[24] Devonian *units associated with acid seeps plus the within-catchment area of wetland-associated unconsolidated Quaternary surficial deposits (Qs) (*Reactive lithology area*); and the multiplicative product of the two predictors (*Expected reactive lithology area exposed to near-surface permafrost)*. Regression model comparisons used adjusted-R^2 and statistical significance of model coefficients (α = 0.05).

Model comparisons revealed that:

1) *Near-surface permafrost probability* model was least accurate (adj-R^2 = 0.41, p_{pfr} = 0.008).
2) *Reactive lithology area* model was slightly more accurate than permafrost alone (adj-R^2 = 0.48, p_{geo} = 0.004).
3) *Expected reactive lithology area exposed to near-surface permafrost* was more accurate than models with either variable alone (adj-R^2 = 0.67, $p_{pfrxgeo}$ = 0.002).
4) Additive model with both variables was most accurate (adj-R^2 = 0.72, p_{pfr} = 0.006, p_{geo} = 0.003).

Additional modeling supported the Fe contribution to tributaries by FRM. To explore the idea that subsurface wetland geology (Qs) contributes measurable dissolved Fe to tributaries, we constructed a model predicting log-transformed dissolved Fe that excluded Qs from *Reactive lithology area*. The permafrost coefficient of this new model remained significant (p_{pfr} = 0.02), but the modified geology coefficient lost significance (p_{geo}* = 0.30). This model explained less variability in dissolved Fe (adj-R^2 = 0.40) than did the model with Qs included in *Reactive lithology area* (adj-R^2 = 0.72). *Expected reactive lithology area exposed to near-surface permafrost* models predicting log-transformed sulfate with *Qs* ($p_{pfrxgeo}$ = 0.16, adj-R^2 = 0.08) and without Qs ($p_{pfrxgeo}$* = 0.0005, adj-R^2 = 0.59) suggested there was no measurable SO_4^{2-} production from Qs, but substantial production from *units.

Water chemistry varies by waterbody type

Among the six waterbody types in the subregional area (Fig. 3, Supplementary Fig. 3), acid seeps displayed the lowest pH (median = 3.1), highest electrical conductivity (EC, median = 2.4 mS cm^{-1}), and most extreme temperatures (1.2 °C at a small streamside acid seep shown in Supplementary Fig. 4 and 20.1 °C at a recently emerged large hillside acid seep shown in Supplementary Fig. 5). Median pH (Fig. 3c) of wetlands (7.5) was identical to stained stream locations (7.5) and lower than Salmon River (7.7), clear stream (7.9), and Kobuk River locations (7.9).

Iron Fe concentrations also varied among waterbody types (Fig. 3a), but differences depended on dissolved versus particulate Fe. Concentration

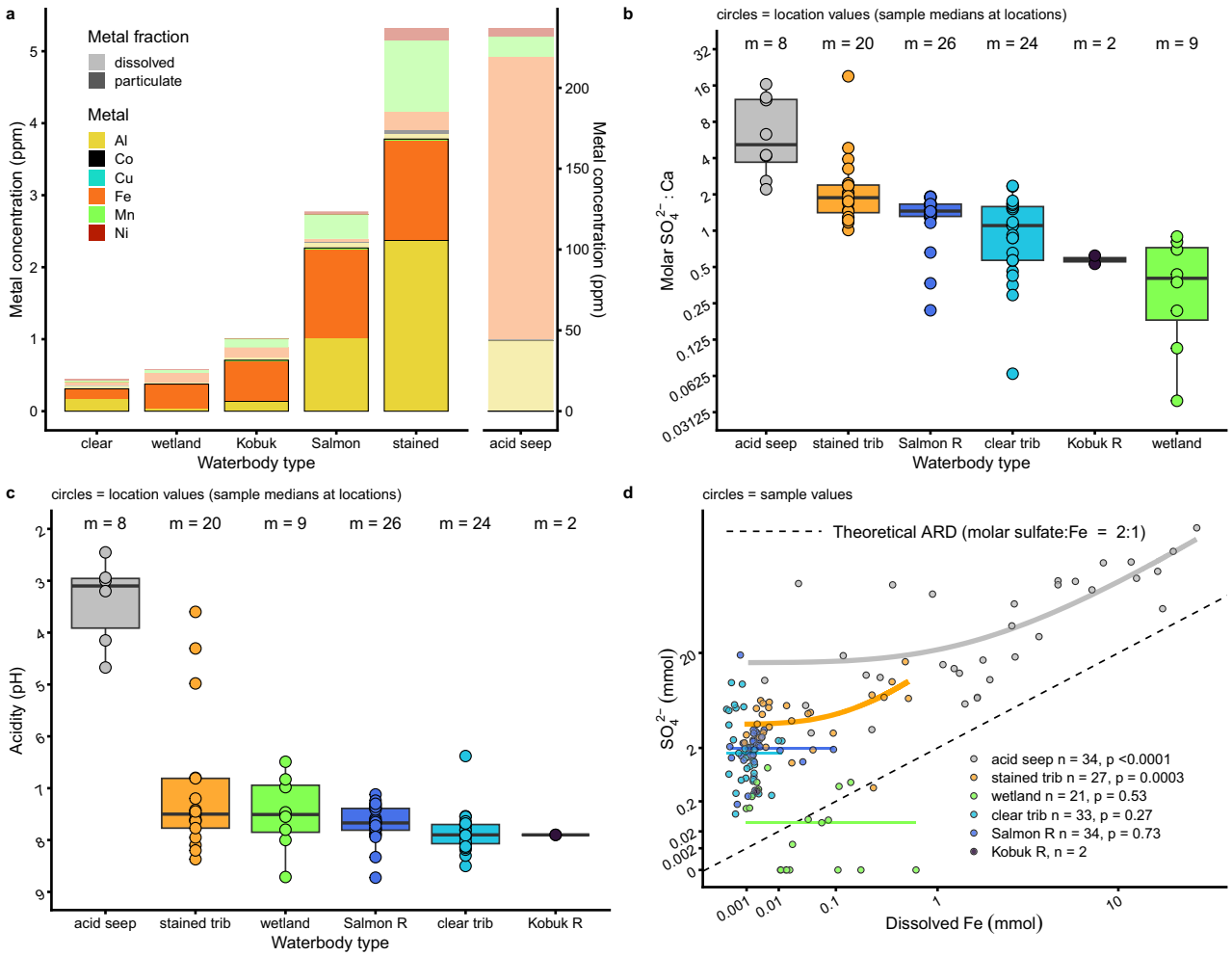

Fig. 3 | Relationships among sulfate (SO_4^{2-}) and ARD products differ by waterbody type. a Metal concentrations by waterbody type. Stacked bars show sum of median concentrations for six metals (Fe, Al, Mn, Ni, Co, Cu), with dissolved (<0.45 µm, lighter shading) and particulate (>0.45 µm, darker shading) fractions. Acid seeps show metal loads on separate scale. **b** Molar SO_4^{2-}:Ca ratios by waterbody type. Circles represent location values (sample medians at locations) with whiskers (vertical lines) extending from box to most extreme data point within 1.5 × IQR of the box edge, where IQR is the third quartile minus the first quartile. Ratios »1 indicate SO_4^{2-} from ARD rather than carbonate dissolution. *m* = sampling locations per type. **c** Acidity as pH by waterbody type. Circles represent location values (sample medians at locations) with whiskers (vertical lines) at 1.5 IQR. Note reversed pH scale. **d** SO_4^{2-} versus dissolved Fe (both axes fourth-root transformed). Colored lines show empirical relationships: regression lines for significant Fe-SO_4^{2-} coupling in ARD sources (acid seeps, stained tributaries; both $p < 0.001$); horizontal segments at median SO_4^{2-} for non-significant relationships ($p > 0.05$) in non-ARD sources (wetlands, clear tributaries, Salmon River; all $p > 0.25$). Dashed gray line shows theoretical ARD stoichiometry (SO_4^{2-}:Fe = 2:1). *n* = sample values per waterbody type. Location values averaged over repeated spatial or temporal samples.

of particulate Fe was calculated as *particulate Fe = total Fe − dissolved Fe*, where *total Fe* was Fe concentration measured from unfiltered samples and *dissolved Fe* was Fe concentration in filtered (<0.45 µm) water samples. Most particulate metals were Fe or Al (Fig. 3a), which together correlated very strongly in Salmon River samples ($r = 0.99$, $n = 10$ samples). When excluding acid seep samples, turbidity (formazin nephelometric units, FNU) was also very strongly correlated with particulate Fe ($r = 0.92$, $n = 41$). Strong correlations held in wetlands, stained tributaries, and the Salmon River but less so in acid seeps and clear tributaries (Supplementary Fig. 6). For non-stained stream and non-acid seep waterbodies, dissolved Fe concentrations (but not Mg, Mn, or Ni) at high discharge in July were greater than concentrations at median discharge in August (Supplementary Fig. 7), consistent with a flush of Fe from wetlands following mid-summer rain events.

Acid seep averages of dissolved Fe (median = 93 ppm) and total Fe (191 ppm) were two orders of magnitude greater than stained and clear stream averages (Supplementary Fig. 3a, b). Dissolved Fe in wetlands was 1.6× higher on average (0.98 ppm, $m = 9$ locations of replicate sample averages) than in stained streams (0.58 ppm, $m = 20$), but total Fe in stained streams was 5× higher (2.0 ppm, $m = 14$) than in wetlands (0.4 ppm, $m = 3$). Between-location variability in both dissolved and total Fe was lower among wetlands than among stained streams.

Sulfate The highest SO_4^{2-} concentration (Supplementary Fig. 3f) occurred in acid seep locations (median = 2787 ppm). There, SO_4^{2-} concentration was 6× that in stained streams (439 ppm), 16× that in clear streams (172 ppm), and over 500× that in wetlands (5 ppm). The median SO_4^{2-} concentration in Salmon River locations (194 ppm) was near the mean of wetlands, clear streams, and stained streams taken together (206 ppm). The median SO_4^{2-} concentration of the Kobuk River (mainstem to Salmon River) was much less (33 ppm). As expected, bivariate relationships between SO_4^{2-} concentration and indicators of ARD (H^+, dissolved Fe, SO_4^{2-}:Ca) in acid seeps and stained stream samples were stronger than in wetland samples (Fig. 3). Median SO_4^{2-}:Ca was highest for acid seep locations (5:1) and lowest for the Kobuk River (4:5) and wetlands (1:3). The median of Salmon River locations (3:2) was midway between stained (2:1) and clear (1:1) streams. The relationship between sulfate and dissolved Fe approached the theoretical molar SO_4^{2-}:Fe = 2:1 ratio in acid seep and stained tributary samples. All non-wetland waterbody types showed surplus

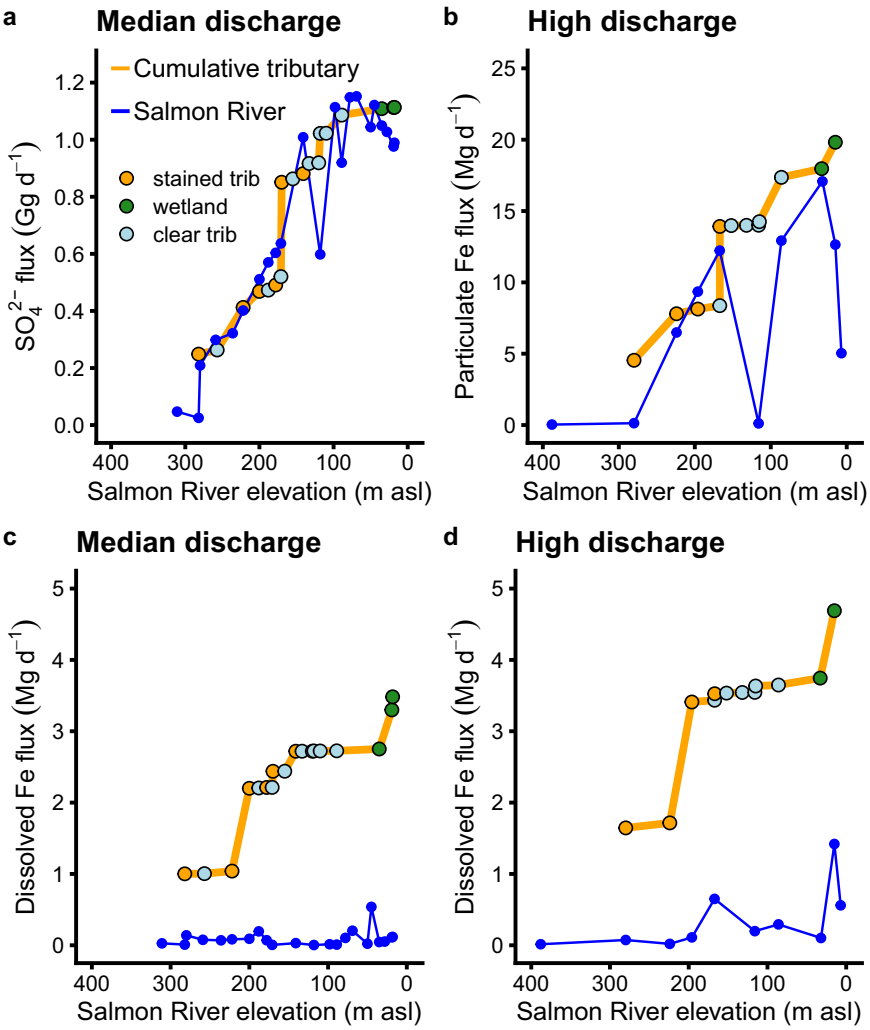

Fig. 4 | Sulfate and iron fluxes along the Salmon River longitudinal profile under median and high discharge conditions. Fluxes calculated from headwaters (400 m asl) to mouth (14 m asl) by multiplying modeled discharge and measured concentrations. Colored points show tributary inputs by source type. Blue line = main-stem Salmon River; orange line = cumulative tributary flux. **a** Mean daily dissolved SO_4^{2-} flux during median flow. **b** Mean daily particulate Fe flux (unfiltered minus filtered <0.45 µm) during high flow. **c**, **d** Mean daily dissolved Fe flux during median (July 19–August 14, 2023) and high (June 30–July 26, 2023) discharge, respectively.

SO_4^{2-}, consistent with Fe precipitation and/or additional sulfate production by oxidation of non-iron sulfide minerals.

Fe and SO_4^{2-} *flux* We calculated particulate Fe and dissolved Fe and SO_4^{2-} fluxes by multiplying their concentrations measured in the water column by co-located discharge estimates (Fig. 4). The Salmon River fluxes of both particulate and dissolved Fe were bimodal (Fig. 4b–d). The upper-elevation maximum particulate Fe flux occurred near treeline at 165 m above mean sea level (AMSL) below a series of stained streams. The low-elevation maximum occurred within wetlands (35 m AMSL). The mid-elevation minimum particulate Fe flux occurred in upland white spruce forest (116 m AMSL) among a series of clear tributaries. Kobuk River total Fe flux (79.2 Mg d^{-1}) exceeded all waterbodies because of its discharge. The average cumulative tributary flux of dissolved Fe was 15–38× Salmon River flux at similar river elevations during median discharge; it was 7–36× Salmon River flux during high discharge (Fig. 4c, d). At high discharge, average input of particulate Fe from cumulative tributary flux was much closer (1.5–1.7×) to Salmon River flux (Fig. 4b) and cumulative tributary input of SO_4^{2-} was approximately equal to Salmon River flux for its entire length (Fig. 4a).

Acid seep hydrogeochemistry varies by bedrock formation

Shales are common sources of ARD whose fundamentally impermeable structure plays a critical role in seep formation. We sampled total dissolved solids ($1.3 \le \text{TDS} \le 18.2$ ppt) and SO_4^{2-} ($1.0 \le SO_4^{2-} \le 12.8$ ppt) in $n = 14$ acid seeps ($2.9 \le \text{pH} \le 4.6$) within the Ikalukrok Creek watershed (Fig. 5a) in September 2020. Seeps were mostly located in Qs[24] within discontinuous permafrost[25]<0.5 km from and downstream of shale-containing Okpikruak, Siksikpuk, and Kuna Formations[24] within continuous permafrost[25]. Seeps downstream of the Kuna Formation displayed high Zn and Fe concentrations; those below the Siksikpuk Formation displayed high Mn concentration. All acid seeps together showed non-significant correlations between pH and log(TDS) ($r = -0.33$, $p = 0.25$) and pH and log(SO_4^{2-}) ($r = -0.33$, $p = 0.25$). These two correlations were significant when excluding seeps nearest to the Kuna Formation (Supplementary Fig. 8). During 2015–2023, pH and TDS were sampled at monitoring station Ikalukrok 207 (Fig. 5a). Among the $n = 8$ acid seeps sampled upstream of Ikalukrok 207, Mn was the most abundant of 10 metals (Al, Mn, Fe, Zn, Ni, Cu, Co, Cd, As, Pb) in all but seep S8 (100 m downhill from Kuna Formation rocks[24]) where Fe and Zn were most abundant (Fig. 5c–f). TDS and SO_4^{2-} were sampled at Ikalukrok 207 during 2009–19 and 2023–24; they correlated very strongly ($r = 0.98$, $n = 148$ samples) with SO_4^{2-} making up 62% of TDS on average (range 27–81%). In acid seeps upstream of Ikalukrok 207, SO_4^{2-} made up >85% of TDS ($R^2 = 0.999$, Fig. 5b). Because SO_4^{2-} was so well predicted by TDS (Fig. 5b), TDS served as a proxy for ARD in the Ikalukrok Creek watershed.

Active layer depth anticipates ARD in streams by one year

Active layer thickness Stream transport of ARD lagged ALT by 1 year. We estimated ALT using GIPL2[29] to model ground temperatures (Fig. 6). GIPL2 was calibrated with data associated with $n = 4$ boreholes (Supplementary Table 2) and boundary conditions of precipitation and air temperature recorded near RDM (Fig. 5a). Demonstrating the tendency of shrubs to trap snow and so warm soils[22,29,30], ALT was substantially deeper below shrub

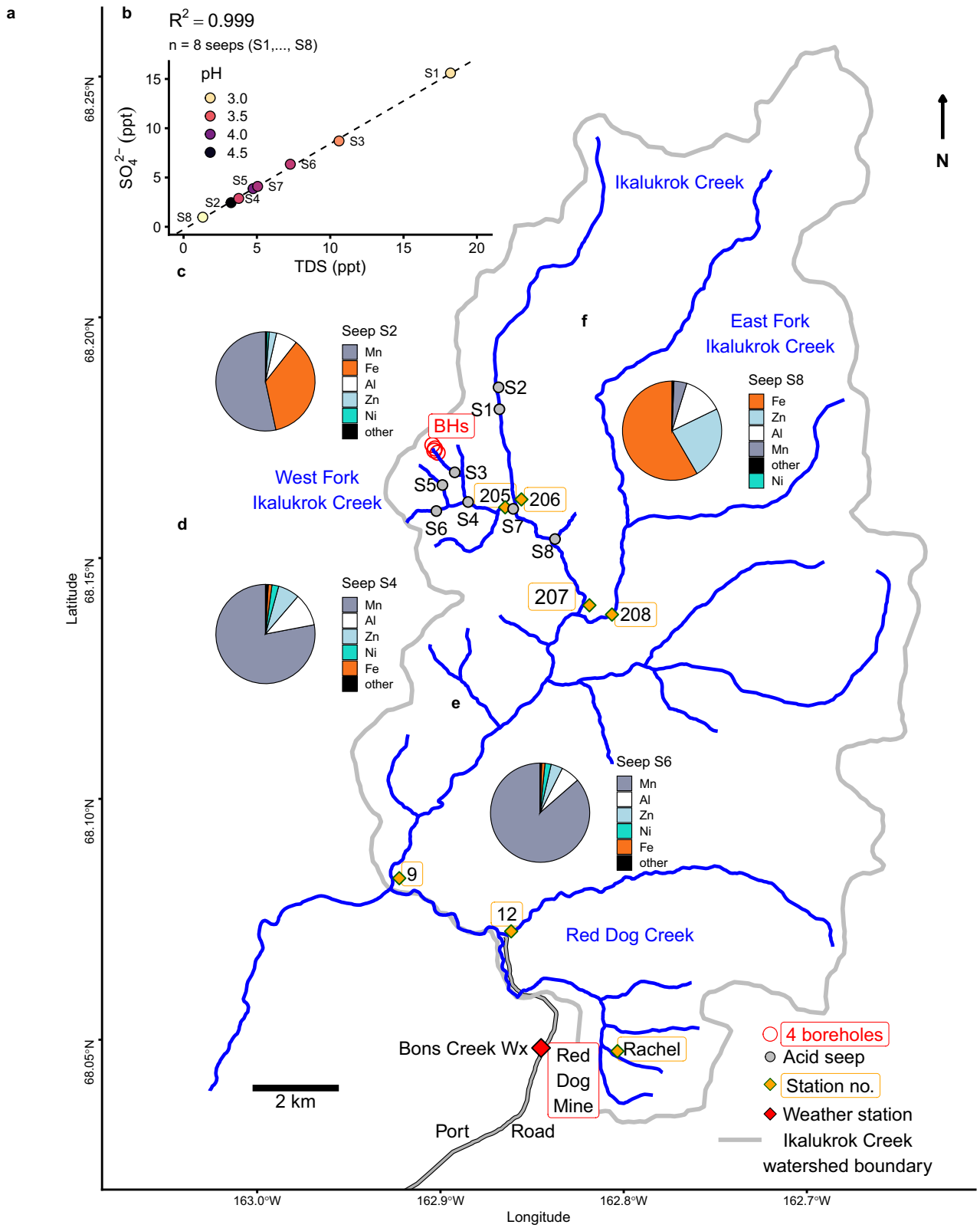

Fig. 5 | Local study area. a Map of Ikalukrok Creek watershed. **b** Regression of SO_4^{2-} on TDS for seeps S1-S8 on map with pH value of seep indicated by point color. Samples collected 9 September 2020. **c–f** Percentage of metals (Mn, Al, Zn, Ni, Fe, Pb, Cd, As, Co, and Cu) from four representative acid seeps upstream of Station 207. Top five most abundant metals named (less abundant combined as "other"). The area of Ikalukrok Creek watershed is 206 km^2.

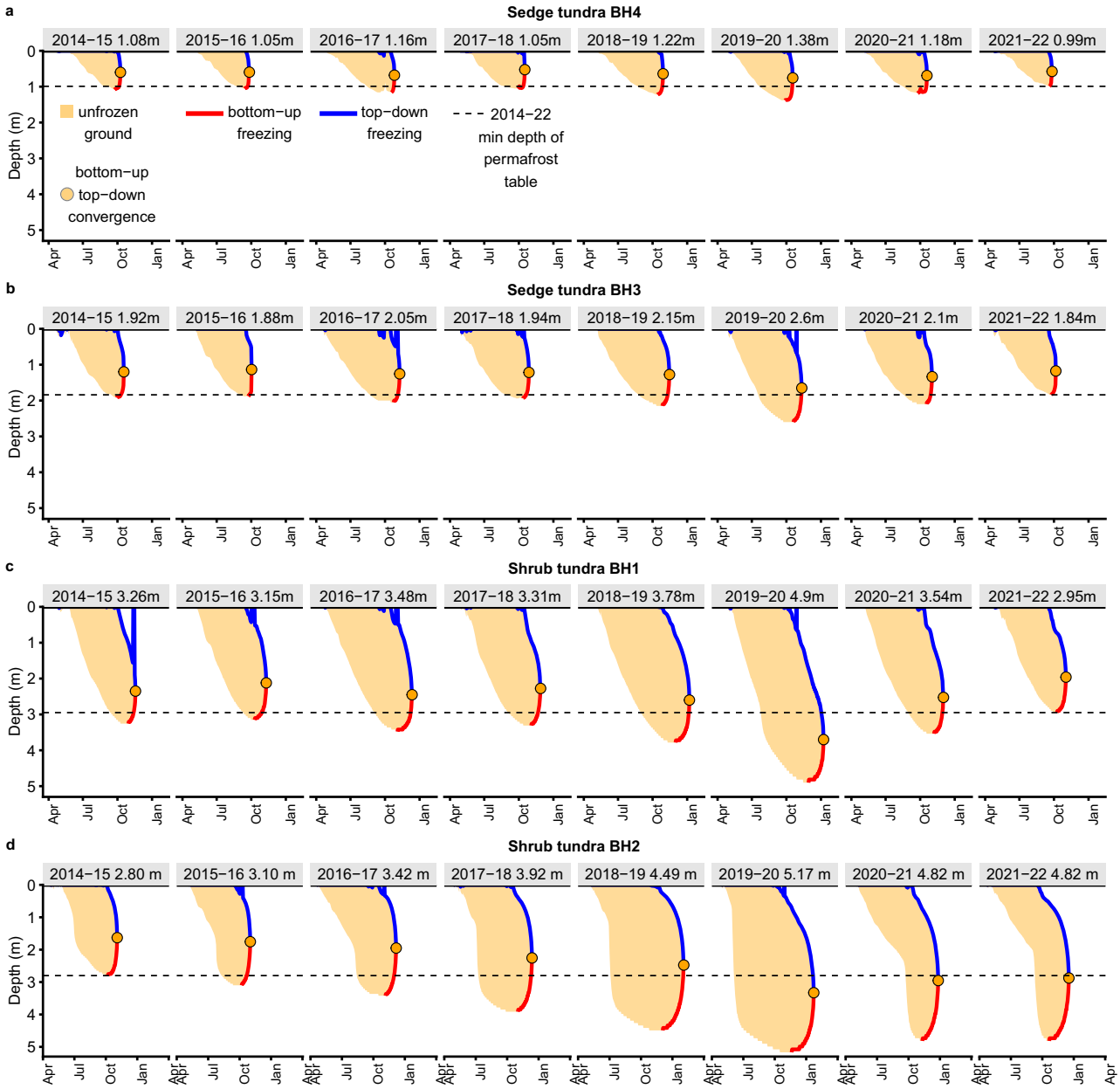

Fig. 6 | 2014–2021 active layer thickness (ALT) dynamics at four boreholes. **a**, **b** GIPL2[29] modeled ALT dynamics beneath sedge meadow tundra. **c**, **d** GIPL2 modeled ALT dynamics beneath low shrub tundra. In **a**–**c** horizontal axis gives days during April of year T through January of year T + 1; in **d** horizontal axis gives days during April of year T through April of year T + 1. Vertical axis gives daily ALT as depth below surface in meters. Dashed lines in each panel indicate shallowest ALT during 2014–2021. Red lines indicate seasonal bottom-up freezing; blue lines indicate seasonal top-down freezing. Tan shading indicates unfrozen ground. Numbers in facet headings give time period and maximum ALT during that period. Dynamics calculated with GIPL2 model using Bons Creek Wx station daily temperature and snow depth. Ground characteristics determined from borehole logs. Boreholes located 47–212 m apart within a 0.45 ha sample area at 377–394 m asl in the headwaters of West Fork Ikalukrok Creek (Fig. 5a). Supplementary Fig. 10 shows ground temperatures for each borehole.

tundra than below sedge tundra. Following a winter of above-average snowfall and a record summertime thaw-index value (Supplementary Fig. 9), the ALTs of individual boreholes (Supplementary Fig. 10) and their mean (Fig. 7a) reached maxima during autumn 2019 (Fig. 6). In autumn 2020, widespread tributary rusting in the Ikalukrok Creek watershed[27] (Fig. 7d) and streams elsewhere in the Brooks Range[4,5] occurred.

Timing of *ARD* In general, TDS at each station during each year was higher during August-October than May-July (Supplementary Fig. 11). TDS at Ikalukrok 207 correlated very strongly ($r = 0.91$, $p = 0.005$, $n = 7$ years) with count of orange-stained Ikalukrok Creek tributaries (Fig. 7d), suggesting TDS can be used as an indicator for ARD. Five kilometers downstream of the boreholes, Ikalukrok 207 recorded peak acidity in autumn 2020 (Fig. 7b), the year when peak TDS occurred throughout the greater Ikalukrok Creek watershed (Fig. 8a). With one exception, monthly TDS at all seven stations and autumn mean pH at Ikalukrok 207 ($r = -0.57$, $n = 8$ year-pairs, $p = 0.1$) were not significantly correlated with concurrent year mean ALT during 2015-2022 (Fig. 9a). In contrast, September and October TDS measures at all stations correlated strongly and significantly with mean ALT of the previous year; with one exception May TDS was not significantly correlated with previous year mean ALT at any station (Fig. 9b). Mean ALT of the previous year correlated strongly and significantly with autumn pH at Ikalukrok 207 (Fig. 7c, $r = 0.96$, $n = 8$ year-pairs, $p < 0.001$) and with count of stained tributaries of Ikalukrok Creek ($r = 0.83$, $n = 6$ year-pairs, $p = 0.02$).

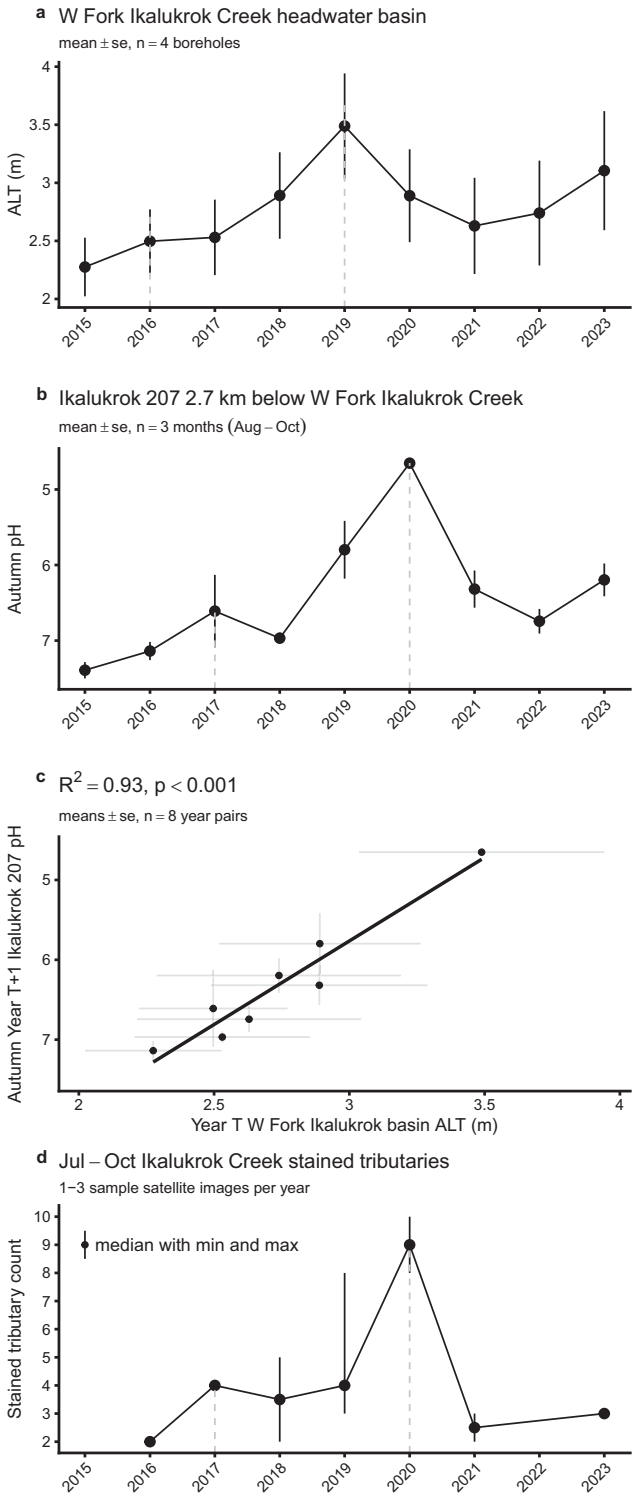

Fig. 7 | Ikalukrok Creek pH and tributary staining lagged ALT by one year. **a** Mean active layer thickness from four boreholes ("BHs" in Fig. 5a) in the West Fork Ikalukrok Creek headwaters peaked in 2019. **b** Mean autumn (Aug-Oct) pH (note reversed y-axis) at monitoring station 207 on Ikalukrok Creek located 5.1 km downstream of boreholes ("207" in Fig. 5a) peaked in 2020. **c** Mean autumn Ikalukrok Creek pH in year T + 1 plotted against mean ALT in year T showed strong, significant linear relationship ($R^2 = 0.93$, $p < 0.004$) **d** Median count of stained tributaries identified on 1–3 m resolution satellite imagery using visible RGB on MAXAR[62] imagery and reflectance indices on Planet[64] imagery. Vertical dashed lines illustrate temporal lags.

Discussion

Geology and permafrost thaw in combination are determinants of where, how, and when Arctic river rusting occurs. Across three spatial scales, results here show iron-impaired streams are strongly associated with sulfide-bearing geologic units and near-surface permafrost conditions. However, at the subregional scale, we identified clear evidence of two distinct pathways operating simultaneously. ARD[11] from upland bedrock sources delivers iron, elevated sulfate, and acid. FRM[12,13] in lowland wetlands[3,14–17] delivers iron with minimal sulfate. The resulting bimodal iron flux in the Salmon River demonstrates this dual-pathway system where both pathways contribute measurably. Stained tributaries draining uplands presented average dissolved Fe of 0.58 ppm with high SO_4^{2-} (439 ppm), indicating ARD dominance. Wetlands presented average dissolved Fe of 0.98 ppm but minimal SO_4^{2-} (5 ppm), indicating FRM dominance. Although both pathways contribute measurably to the Salmon River's bimodal flux profile, the similarity of wetland and Kobuk River chemistry (EC, SO_4^{2-}, total Fe, dissolved Mn, SO_4^{2-}: Ca, Supplementary Fig. 3b–f) suggests FRM may dominate at the larger catchment scale.

Previous studies[2–9] have hypothesized causal linkages between permafrost thaw and stream rusting. Results here advance that hypothesis with modeled ALT and measured TDS on seven streams over 8 years. The 1-year lag between active layer depth and downstream ARD product concentrations could be explained by solute transport that slows (or even stops) following freeze-back in November and then begins with seasonal thaw in April, increasing over summer into fall. Our 2015–2022 TDS time series included May–October monthly measurements for most stations. An April 2016 TDS sample from Rachel Creek was the lowest for that year (80 ppm), and TDS averaged across monitoring stations during August–October was 1.2–3.4× TDS during May–July, indicating greater late than early thaw season release of ARD (Supplementary Fig. 11). Field observations and 1–3 m resolution imagery of Fe precipitates on top of aufeis (Supplementary Fig. 4) also suggested that November–March ARD release is minimal, except where taliks occur in some areas during some years[28] (e.g., Kutuk River; Dirk Nickisch, fixed-wing aircraft pilot at Coyote Air Services, oral communication, 2021).

Taken together, these lines of evidence and ground temperature modeling (Fig. 6) support the idea that autumn freezing air temperatures occurring slightly after maximum ALT is reached initiate top-down freeze-back. This ground refreezing seals ARD somewhere in the active layer (e.g., at the top-down/bottom-up convergence) until winter ends[2], when thaw liberates ARD products that mobilize downstream. One-year time lags between warming and aufeis formation in Arctic Alaskan rivers have been related to talik development and subsurface hydrology transport and connectivity[36]. Similar processes may occur with ARD, as well as buffering capacity of surrounding rocks, travel distance from subsurface to stream, and the mechanical frost fracturing of rock in the deepened active layer.

In our study, OCWs appear concentrated in sulfide-ore deposits hosted in Paleozoic platform carbonates or deep basin shales and metasedimentary formations with acid seeps concentrated in Devonian pyritic schists and shales. Where lithology and permafrost allow, these patterns may extend elsewhere in Alaska[3–5,20,27,29,31], nearby Canada[2,10,32–34], Scandinavia[14–17], and alpine settings[6–9,35]. A previous study also identified bedrock type as a control of sulfate flux in northwest Canada[10]. Widespread increasing sulfate there derives primarily from pyrite oxidation[10,30,32–34], suggesting that river rusting could be ongoing or incipient. Identifying these formations provides a necessary first step in projecting which watersheds will be vulnerable to chronic metal loading[5] under climate change.

Near-surface permafrost thaw initiates rusting, conditional on geologic setting. Within and adjacent to KOVA, acid seeps were 22× more likely to occur in sulfide-bearing units with near-surface permafrost probability[26] exceeding 50% than at random points. A high probability of near-surface permafrost implies ALT will more likely respond to atmospheric warming, deeper snow, or changing hydrology. A low-probability indicates deep permafrost (or no permafrost) where thaw is less likely than in shallow permafrost under similar conditions of warming. Statistical models of

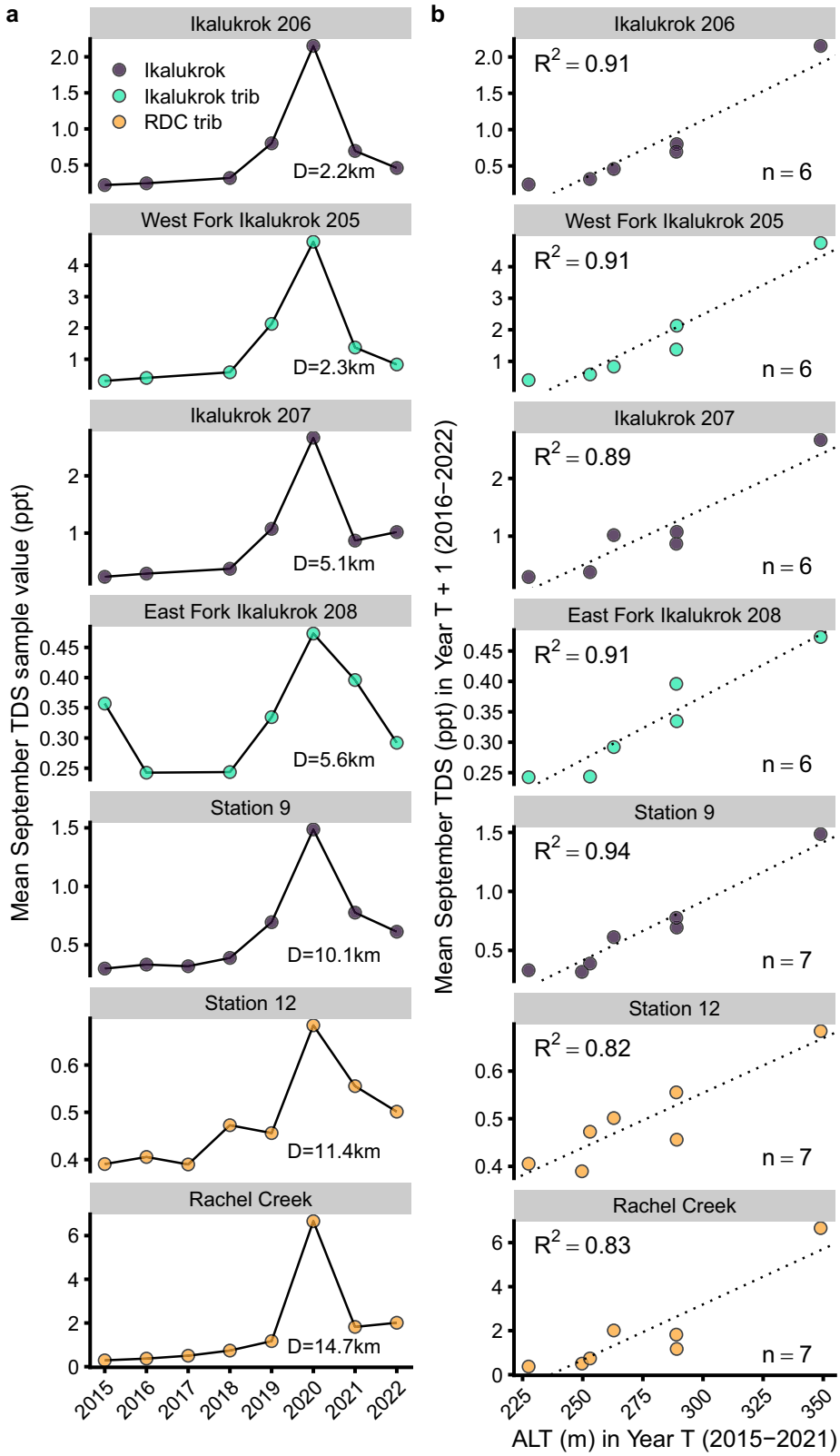

Fig. 8 | 2015–2022 September total dissolved solids (TDS) in Ikalukrok Creek watershed lagged ALT in Ikalukrok Creek headwaters by one year. **a** Mean September TDS recorded at each of seven monitoring stations located $2.2 \le D \le 14.7$ km distant from boreholes (Fig. 5a). **b** Mean September TDS in year T + 1 plotted against mean ALT in year T shows strong linear relationship (simple linear regression: $0.82 \le R^2 \le 0.94$, $n = 6$–7 year-pairs in each plot). Locations of stations shown in Fig. 5a.

dissolved iron in KOVA streams were most accurate when they incorporated geologic unit[24] (e.g., catchment areas included pyritic schists, shales with diagenetic pyrite, and marbles of Paleozoic age, as well as Quaternary surficial deposits underlaying wetlands[3,14,15]) and near-surface permafrost probability[26] and were more accurate than models with either variable alone. The most accurate model explained 72% of variance in dissolved iron concentrations, demonstrating robust predictive capability for identifying vulnerable watersheds. However, models based on geologic mapping require local calibration.

Regionally, OCWs were nearly four times more common in areas mapped[23] as potential zinc-sulfide deposits within discontinuous permafrost[25] than expected by chance. This association weakened in

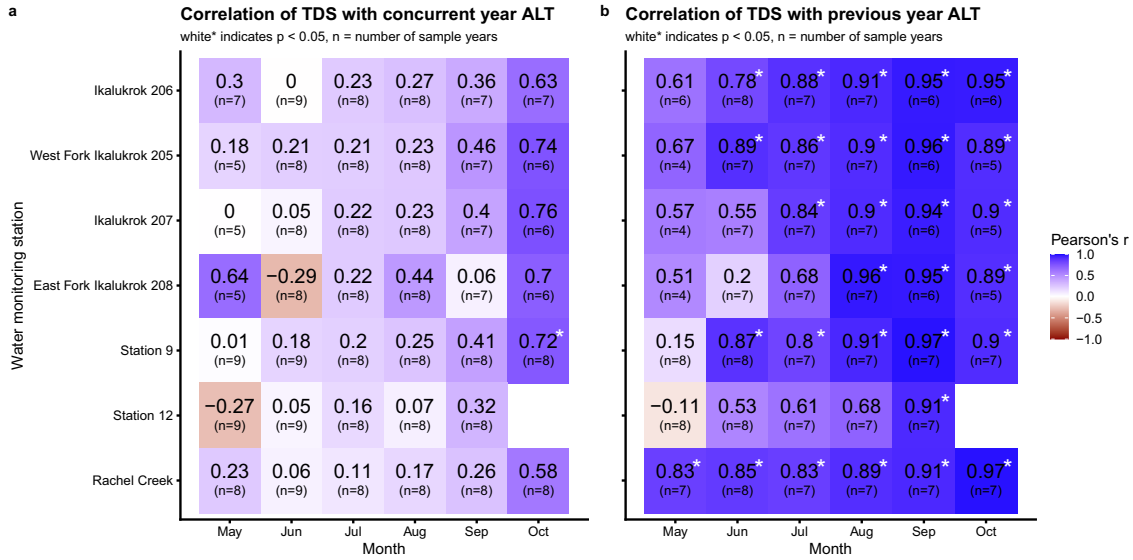

Fig. 9 | Strong correlations of lagged year TDS and ALT contrast with weak correlations of concurrent year TDS and ALT. a Heat map of Pearson's correlation between same year TDS and ALT by month and stream monitoring station. **b** Heat map of Pearson's correlation between year T + 1 TDS and year T ALT by month and stream monitoring station. In both panels, Pearson's r displayed as $-1 \le r \le 1$ with number of years (n) used to determine correlation given in parentheses and white asterisk denoting significant ($p < 0.05$) correlations. Lack of white star indicates non-significant correlation ($p \ge 0.05$). Locations of stations shown in Fig. 5a.

continuous permafrost, where deeper, colder ground is more resistant to thaw. However, in some settings, ice content may be more important for thaw than percent cover of permafrost, such as in cold, mountainous environments with coarse soils of ice-poor permafrost[22] that thaws with less warming.

Active layer deepening coincident with warm summers and deep snowpacks is also consistent with snow insulation promoting thaw[22,29,30], where vegetation plays a key role. ALT in shrub tundra reached twice that in sedge tundra, emphasizing that vegetation mediates snow trapping and thaw depth[22,29,30]. Increasing air temperature and winter precipitation are associated with sea-ice loss[37]. We identified more orange-colored water bodies nearer the Chukchi Sea (where sea ice loss is leading to increased and more variable snowfall) than near the Beaufort Sea (where sea ice loss has been less rapid)[37]. These integrated processes create a predictable sequence: anomalously warm years followed by deep snowpacks initiate deep thaw, generating ARD products that appear in streams the following year.

Previous localized studies[2,6–9,35] have suggested links between permafrost degradation and ARD appearance. In Yukon, Canada, removal of insulating sediments overlying permafrost triggered ARD from underlying shales, but ARD did not occur in an adjacent waterway where sediment removal had not taken place[2]. Another paired comparison in the Italian Alps[35] demonstrated a steeply increasing seasonal trend in sulfate over 8 years in an alpine pond in a permafrost-affected basin, but found no such trend in a nearby pond outside the affected basin. In the mountains of Colorado, USA, statistically significant increasing trends in metals, sulfate, and mean air temperatures suggested permafrost thaw causes ARD[6,7]. Similarly, historical aerial imagery of the Spanish Pyrenees showed an elevational rise in ARD consistent with warmth-driven permafrost thaw[8], while ARD followed glacial recession in the Peruvian Andes[9].

Our study extends previous studies by quantifying associations across spatial scales and multiple years. It also demonstrates that both upland ARD and lowland FRM contribute measurably to iron loading, and that ARD products can correlate strongly to previous year active layer depth estimated from measured ground temperatures (pH: $r = -0.96$, TDS: $r = 0.97$). These temporal results explain a near Brooks Range-wide observation of rusting in 2020[4] that followed the unprecedented permafrost instability of 2019[28], when a thermal loss index approached zero for the first time in Arctic Alaska measurement history.

Results here further support two feedbacks proposed[2] within a Devonian shale setting near the Arctic Circle: *Where acid seeps kill vegetation, solar absorption increases and thickens the active layer* and *exothermic reactions add heat to the system*. We identified a large acid seep with dead zones that expanded from 0.5 to 3.6 ha over 8 years (Supplementary Fig. 5a) and measured acid seep water temperatures as high as 19.6 °C (Supplementary Fig. 5b). These feedbacks suggest that once initiated, ARD can become self-sustaining—a concern for watersheds entering impairment that underscores the importance of identifying climate refugia for aquatic organisms in Arctic environments.

Additional aquatic disruption can result as ARD delivers dissolved metals both directly from sulfide oxidation[6–11] and indirectly (as with aluminum) through acid leaching of other mineral phases[8,9]. Sulfate and some metals can persist for kilometers downstream[5], presenting chronic toxicity risks to aquatic organisms[5,6,8,27]. FRM delivers primarily iron that rapidly precipitates upon oxygenation, threatening habitat through substrate smothering. Both pathways contribute substantially to mainstem loading of iron, the fate of which depends on its phase (dissolved vs. particulate)[6–9].

We interpret the observation that an increase in stream discharge increases Fe concentrations from non-stained streams—but not from stained streams—as further evidence that FRM is an important and widespread source of Fe (Supplementary Fig. 7). Previous ARD studies did not find increases in ARD products at higher discharges[6–8] because ARD products are generally transported by deeper groundwaters. The Kobuk River is mainstem to the Salmon River and one of the largest rivers in northern Alaska with total Fe flux = 79 Mg d^{-1}. Its chemistry included low sulfate and low EC, a chemistry similar to wetlands that further highlights the importance of FRM as an iron source (Supplementary Fig. 12).

Dissolved Fe flux in a river can remain substantially less than cumulative tributary contributions, while particulate Fe flux can simultaneously match or even exceed cumulative contributions. These mismatches occur because Fe(II) precipitation as Fe(III)(oxyhydr)oxide, its settling, and its aggregation (e.g., coprecipitation with aluminum) can together strip dissolved Fe from river reaches between tributaries[9]. Our results imply that buffering, settling, and dilution can all reduce Fe flux, particularly of dissolved Fe. However, suspended particulate Fe can continue downstream, maintaining turbidity and harming nearby aquatic ecosystems. Evidence[5] from the Kotzebue Sound fishery in northwest Alaska downstream of the

Salmon River indicates that salmon populations may be affected by rusting effects on eggs and juveniles. In contrast to diminishing populations of aquatic organisms such as fish and macroinvertebrates[5], fertilizer effects of iron on aquatic and nearshore ocean environments[38] could lead to downstream algal blooms.

Permafrost thaw also mobilizes dissolved organic carbon that can fuel greenhouse gas production in downstream aquatic systems. While our study focused on metal chemistry, the processes documented here likely enhance climate feedbacks through $CaCO_3$ reactions with ARD and consequent carbon flux[10,32,33] and through FRM-mediated carbon export[14–17,39,40]. Viewed from a wider ecosystem and Earth system perspective the balance of Fe(II) and Fe(III) in each waterbody type and carbon cycling via Fe-organic complexed matter in wetland-derived waters[14–17,39,40] versus ARD-derived[10,20,32,33] ones are important but currently unknown.

Conclusions

Temporally, the 1-year time-lag between active layer depth and ARD flush offers a potential early warning of stream degradation. Very warm summers with deep snowpack can signal widespread rusting the following year. Monitoring ground temperatures in strategic locations could provide advance notice of impending ARD, allowing managers to assess fisheries impacts. Assessments could be included in fisheries modeling as warm events may reduce juvenile survivorship the following year when ARD and FRM products arrive to downstream aquatic ecosystems, impairing gill functioning and passivating habitat[4,5,27].

Spatially, odds ratios and statistical models offer predictive power by providing a practical framework of evaluation. Streams draining Paleozoic sedimentary rocks (particularly shales) in discontinuous permafrost zones could be prioritized for monitoring as climate warming continues. Both migratory and resident fish spawn in watersheds with those geologic and permafrost conditions[41]. Watersheds without metal-sulfide-bearing geology in continuous permafrost could be protected as climatic refugia to future-proof populations of Arctic aquatic organisms. The strong correlations we demonstrate (e.g., $r > 0.9$ between previous year's ALT and subsequent ARD products) provide quantitative support for these management considerations.

Much remains for future research. Our own observations of Ikalukrok Creek show a dynamism to rusting, and historical names throughout the Brooks Range[42] (e.g., Ferric Creek, Fire Creek, and Ivishak River, meaning "red river" in Innupiaq) demonstrate previous rusting. Well-defined layers of detrital opaque Fe minerals (45–250 μm), principally weathered magnetite (Fe_2O_3) and hematite (Fe_2O_3), have been dated to the Medieval Warm Period (800–1100 years before present) in Chukchi Sea sediment cores[43], suggesting Arctic rusting may have occurred during a warming event that lasted 300 years. Iron profiles could potentially serve as proxies for past climate in permafrost regions. More generally, given permafrost occurrence, geography, and geology, the quantitative balance of iron flux of ARD versus FRM would be informative. The effects of ARD are striking and important but in Arctic and subarctic ecosystems anoxic soils are widespread. As with the Kobuk River (Supplementary Fig. 12c), wetlands may well contribute Fe(II) flux (Supplementary Fig. 12a,b) along thousands of kilometers of Arctic rivers, acting as the largest source of iron flux. The effects of FRM on Alaska's Arctic Slope (Supplementary Fig. 13) where thawing permafrost is qualitatively changing tundra landscapes[44] used by multiple fish species for spawning[45] could be widespread and substantial. These and other topics provide ample—and important—future research directions.

Methods

Overview

To investigate causal pathways among warming air and soil temperatures, snowpack depth, thawing permafrost, lithology, and stream discharge that may determine the spatial and temporal occurrence of orange streams and acid seeps, we focused on three study areas in northern Alaska (Fig. 2) at three spatial scales. The first was the regional defined as the Brooks Range. We digitized around those features located on USGS 1:250,000 quadrangles identified as belonging geographically[42] to the Brooks Range. As calculated in a geographic information system (GIS), the regional study area encompassed 2.41×10^5 km² (Fig. 2a). The second spatial scale was the subregional scale, defined as the Salmon River watershed in KOVA, the adjacent Tukpahlearik Creek watershed above its confluence with the Omar River, and the adjacent Timber Creek watershed above 103 m above mean sea level (m asl). The subregional study area encompassed 2.01×10^3 km² as calculated in a GIS (Fig. 2c,e, and Supplementary Fig. 4). The third spatial scale was the local scale, defined as Ikalukrok Creek upstream and including portions of Red Dog Creek. The local study area encompassed 2.01×10^2 km² as calculated in a GIS (Fig. 2c,e, and Supplementary Fig. 4).

Alaska's Brooks Range (<2800 m asl) separates Arctic from interior climates, tundra from boreal ecosystems[46], and continuous (90–100% land area frozen) from discontinuous (50–90%) permafrost[22]. Schist, shale, and carbonate lithologies that host sedimentary exhalative (SEDEX) deposits and Mississippi Valley type (MVT) deposits of potential sulfide-mineral ores extend over much of the range[23] (Fig. 1a). The last glacial maximum covered nearly all[47] the Brooks Range in Alaska, but ongoing glaciation is minimal[48]. KOVA and adjacent watersheds is characterized by sulfide-mineral content in its uplands (Fig. 2c), wetlands in its lowlands[49] and a broad array of geologic formations and ecosystem types[49]. The third area near RDM is characterized by high sulfide-mineral content[50] and has been monitored with spot samples of water quality[51–58]. Observations and measurements from these three areas provide an integrated framework for understanding how climate change affects Fe-loading into aquatic systems.

Climate data and thermal indices

Kotzebue air temperature Located on the Chukchi Sea, the weather station (Wx) in Kotzebue, AK at the Kotzebue Ralph Wien Memorial Airport (GHCND:USW00026616) at 66.8857, -162.6068, 3 m asl has the longest running air temperature (airT) record in northwest Alaska and captures climate dynamics associated with the Chukchi Sea that affect the Brooks Range environment. We downloaded the 1897–2023 Kotzebue daily record of instrumental temperatures from ref. 59 and calculated the mean daily air temperature as T = (max daily temperature + min daily temperature)/2.

Kotzebue air temperature gap filling We restricted thermal indices to 1941–2023, avoiding data gaps in airT pre-1941. The Kotzebue sensor displayed a 1–3 °C bias from 1 May to 9 September 2019 (verified by a radiosonde installed September 2019). We replaced 1 May to 9 September 2019 airT by applying month-specific regressions of Kotzebue T (airT_Kotz) on airT_Noak from a Wx station (Mt. Noak RAWS[60]), 33 km NNW of Kotzebue (67.1413, -162.994, 255 m asl). We chose a multiple regression approach with month treated as an additive factor variable because bias varied by month. Models with interaction between month and T_Noak (ΔAIC = 3.1), or with year as a random factor (ΔAIC = 0), performed no better than the additive model (ΔAIC = 0.8).

Onset of freezing and thaw Following established methods[61], we defined initial onset of freezing date, d_f, as the first day each year when $T < 0$ °C and the following 7-day mean of T was also <0 °C. The d_f in year Y-1 provided the start of an autumn-to-autumn interval and d_f in year Y provided the interval end. Using airT between successive initial onset of freezing dates (autumn-to-autumn interval) associated with airT_Kotz, we calculated three indices: (1) an annual thawing index (ATI > 0) of year Y, calculated as the degree-day sum of airT >0 over the autumn-to-autumn interval ending in year Y; (2) an annual freezing index (AFI > 0) of year Y, calculated as the absolute value of the degree-day sum of airT <0 over the autumn-to-autumn interval ending in year Y; and their difference as annual thermal loss, AFI–ATI (Fig. 1).

Regional mapping of orange-colored waterbodies

We located 205 locations of orange-stained streams, rusting rivers, and acidic seeps (those colored orange or with dead vegetation) across Arctic Alaska (Fig. 2a) using an opportunistic approach, including field-transects, crowd-sourcing, and satellite-image interpretation. Most locations were identified by an orangish color in sediments and/or orangish hue to water

that was formerly clear; brownish streams were not considered stained. Many, but not all, OCWs had very high-resolution (3 m or better resolution) satellite imagery showing that they had been clear at some point[4] as far back as 2008; however, previous to 2008 imagery was not available to distinguish. It is known that OCWs located as tributaries along the Salmon and Ivishak Rivers, as well Ikalukrok, Fire, Drenchwater, and Ferric Creeks have produced ARD in the past.

During Jun-Aug 2019–2024, we traversed by foot and packraft 3500 km of the Brooks Range, opportunistically geolocating stream rusting and acid seeps as we encountered them. Beginning with field-identified locations, we searched on satellite scenes upstream of and nearby other orange streams, locating where their color emerged by browsing multi-band imagery from 2005 to 2024, including Ikonos[62] (3 m), GeoEye[62] (1–2 m), WorldView[62] (1–3 m), Sentinel-2[63] (10 m), and Planet[64] (3 m). Image interpretation used Google Earth Pro[65], Esri Wayback[66], MAXAR[62], Planet Labs[64], and Copernicus Browser[67]. We applied band-filtering to facilitate identification of sites using normalized pixels from Sentinel-2 scenes captured 13 Jul 2023 and calculated as:

normalized_value = (pixel_value – scene_min_value)/(scene_max_value – scene_min_value)

where 0.07 <normalized_blue <0.09, 0.09 <normalized_green <0.1, 0.07 <normalized_red <0.11, and 0.1 <normalized_NIR < 0.18.

Spatial association analysis: To quantify associations between OCWs and geology/permafrost combinations, we calculated odds ratios comparing observed proportions of OCWs within each category to expected proportions based on regional availability. Specifically, for each combination of geology (within versus outside Zn-ore polygons[23]) and permafrost zone[25] (continuous, discontinuous, sporadic), we calculated the odds ratio as:

$$\text{odds ratio} = \text{observed odds}/\text{expected odds}, \quad (3)$$

where

$$\text{observed odds} = \text{observed proportion}/(1-\text{observed proportion}) \quad (4)$$

and

$$\text{expected odds} = \text{expected proportion}/(1-\text{expected proportion})). \quad (5)$$

For example, if Zn-polygons within discontinuous permafrost comprised 9% of the study area but hosted 25% of OCWs, the odds ratio = (0.25/0.75) / (0.09/0.91) = 3.4. Values > 1 indicate OCWs are more common than expected; values < 1 indicate OCWs are less common than expected. We applied the same approach to acid seeps ($n = 62$) in the subregional study area, comparing their distribution across geology (*units vs. non-*units) and near-surface permafrost probability (<50% vs. >50%).

Geologic setting

Mineral exploration has identified several ore deposits in the Brooks Range, an area that includes one of the most prolific Zn districts in the world. One is the Red Dog clastic-dominated (i.e., SEDEX) deposit, 10 km south of the local study area and 115 km northwest of the subregional study area. The Red Dog deposit was discovered by its oxidized acidic seeps in the early 1950s and contains abundant lead (Pb) and zinc (Zn), hosted largely in sphalerite and galena with pyrite ± marcasite as co-existing sulfide minerals[68–70]. Red Dog deposits are the largest known accumulations of sulfides in the region. The upper Mississippian Ikalukrok unit hosts its SEDEX mineralization. The Re-Os dates of the sulfide minerals constrain their formation from 339.1 ± 8.3 Ma to 333.0 ± 7.4 Ma[70], younger than host rocks underlying the acid seep formation in the subregional study area and nearly identical to the local study area geology. However, a geologic survey[23] did include the SRSA within prospective SEDEX mineralization (Fig. 2a).

Another large regional accumulation of sulfide minerals occurs in the Ambler volcanogenic massive sulfide district, 150 km SE of the subregional study area. Several Ambler deposits reside throughout Devonian to Mississippian stratigraphy, but most mineralization resides within the Devonian-aged sequence (metavolcanics and metasediments) and Devonian to early Mississippian Bornite carbonate sequence[71]. Pyrite, chalcopyrite, galena, and sphalerite with lesser tennantite-tetrahedrite ± pyrrhotite, bornite, and arsenopyrite[71] largely form Ambler's massive-sulfide deposits.

A third mineral deposit in the area is carbonate-hosted within Devonian-aged dolostone, similar to those underlying the subregional study area, exemplified by the Omar deposit[72] located 25 km west of the KOVA. Mineralogy at the Omar deposit is dominated by chalcopyrite and bornite, although Fe-sulfide minerals and galena are mentioned, but not specified, nor are abundances reported. The Omar area deposits are carbonate hosted[72], differing from Red Dog SEDEX, giving a natural buffering ability for streams like Tukpahlearik and Timber creeks.

The areas where we sampled acid seeps in the upper Salmon, Tukpahlearik, and Timber Creek watersheds of the subregional study area during Jul and Aug 2023 field campaigns are underlain predominantly by undivided Devonian to Ordovician metasedimentary and metavolcanic rocks of Tukpahlearik Creek interbedded with marble of Tukpahlearik Creek[24], or the early Paleozoic light grey to white marble that has been thrust on top of the Tukpahlearik Creek rocks[24]. Forming the headwaters of stained tributaries with elevated Fe and other elements that drain into the Salmon River is Devonian to Proterozoic grey to dark-grey pelitic quartz-mica schist interbedded with lesser calcareous schist and mafic lenses[24].

Subregional sampling

The subregional study area included the Salmon River watershed and the adjacent Tukpahlearik and Timber Creek watersheds to the west and outside the KOVA. Within this study area, we classified sample sources (Fig. 3) with six classifications:

Acid seeps. Seeps were considered as sources of water emerging from the ground. Acid seeps were seeps that were either low in pH (e.g., pH <5.5) or as high as 6.7 but with clear evidence of having been much lower by virtue of extensive blackened vegetation or bleached shrub stems (Supplementary Figs. 4 and 5). Acid seeps included streamside seeps in creek bottoms with staining of orange, white, or blueish hues, and hillside seeps which in some cases appeared as newly emergent with very low pH (e.g., <4), clear water coloration, and live green vegetation. Levels of EC and pH in acid seeps were often highly variable over short intervals of time and space.

Stained tributaries. Streams with sediments stained orange, whitish, or bluish. Water could be either turbid or clear. Usually downstream or downhill of known acid seeps. Green benthic algae and macroinvertebrates were generally absent or much reduced.

Clear tributaries. Streams without stained sediments and with clear water and green benthic algae, macroinvertebrates, and often fish present.

Wetlands. Vegetated wetlands and the surfacing soil water, streams, rivers, lakes and ponds within or draining them (Supplementary Figs. 12 and 13). Most were vegetated by sedges (e.g., *Carex* spp. and *Eriophorum* spp.), willow shrubs (*Salix* spp.), and occasionally black spruce trees (*Picea mariana*) and alder shrubs (*Alnus* spp.).

Salmon River. The Salmon River, a Wild and Scenic River in KOVA that has historically functioned as an important anadromous and ambidromous fish spawning river[5]. Ungaged.

Kobuk River. The Kobuk River (Supplementary Fig. 12c), mainstem to the Salmon River, flows roughly 500 km from mountain headwaters to Chukchi Sea. A USGS streamgage station[73] (15744500) is located 35 km downstream of the Salmon River mouth. The nearest Kobuk River water sample collected for this study was 22 km upstream of the USGS streamgage.

Field campaigns

KOVA offers few reliable locations to land fixed-wing aircraft within its boundaries >300 km from Alaska's road system. Access is by National Park Service (NPS) permitted helicopter or on foot from outside the park. In July and August 2023, we accessed the park on foot, sampling outside the park and observing streams and acid seeps en route to the park. In Aug 2023, an

NPS-permitted helicopter also supported access to the Salmon River headwaters. During both campaigns, we descended the river from its headwaters to its mouth using small inflatable packrafts. In July 2023, we descended the Kobuk River to the community of Kiana (66.9731, -160.4271). Based on USGS streamgages[73] (Supplementary Table 3) on the Kobuk River (Site number 15744500) and Wulik River (Site number 15747000) discharges, the field campaign in Aug 2023 occurred during median discharges and in July 2023 occurred during high discharge with Dahl Creek (Site number 15743850) discharge at 90th percentile, Wulik River at 80th percentile, and Kobuk River near 95th percentile.

We define *samples* as individual water samples or point measurements (e.g., pH, temperature) and *locations* as places we sampled during two field campaigns (July and August 2023) or at large acid seeps with multiple samples across an individual seep's extent, generally within 100 m of each other. The variable value at a location was calculated as the average of sample values for that variable from that location. Every sample measurement reported here has a location; some locations have multiple samples, as in up to two for field campaigns on the Salmon River and its tributaries, and as many as $n = 15$ for very large acid seeps.

Water sampling

In July 2023, we collected filtered (0.45 µm disc filters) and unfiltered samples but only collected filtered samples in August 2023; 2023 samples were acidified at the time of collection with 1% nitric acid in August and 2% in July 2023. At each sample location, we measured pH, specific conductivity (EC), and temperature. In July 2023, we used a YSI ProDSS multi-parameter meter (calibrated in the laboratory prior to departure) and included turbidity (FNU). In August 2023, we used a Thermo Orion A325 with electrodes for pH (Thermo Scientific 9106BNWP, calibrated each morning in the field) and EC (Thermo Scientific 013010MD).

Metal concentrations from samples passing through a 0.45 µm filter and subsequently acidified are referred to as "dissolved" metals. Metal concentrations from unfiltered samples are referred to as "total" recoverable metals. Acidification of unfiltered water samples is not expected to liberate metals from all particulates (e.g., clay minerals and silicates) but is expected to release metals from the most bio-available particulates, such as Fe and Al oxyhydroxides. Particulate metal concentrations were calculated as particulate Fe = total Fe − dissolved Fe, where total Fe was Fe concentration measured from unfiltered samples and dissolved Fe was Fe concentration in filtered (<0.45 µm) water samples. The same approach was applied to calculate particulate Al and other metals.

Laboratory processing and analysis

At the University of California Riverside, we measured major and trace element compositions of the water samples using standard methods for inductively coupled plasma mass spectrometry (ICP-MS). An Agilent 7900, single quadrupole, ICP-MS, fitted with an Agilent ISIS integrated sample introduction system, analyzed samples at 10× dilution in 2% nitric acid. Instrument outputs were calibrated using matrix matched, multi-element standards that were freshly prepared in-house. All solutions were prepared using trace-metal grade nitric acid and 18.2 MΩ water. Various QA/QC protocols were applied, including periodic analysis of standard reference material NIST1640a throughout the runs and online introduction of multielement internal standards. Within-run reproducibility was generally within ±5% for all elements. Long-term accuracy/reproducibility studies indicate an accuracy of ±5% for major elements and ±10% for trace elements. Recovery of all measured elements in the standard reference material NIST1640a was within these tolerances.

Statistical modeling of dissolved Fe in Salmon River tributaries

To model dissolved Fe concentrations in Salmon River tributaries, we selected those $n = 14$ tributaries with pH >5 sampled in August 2023. We defined predictor variables at the catchment scale using GIS analysis with probability of near-surface (<1 m) permafrost occurrence within each tributary catchment extracted from a 30 m raster product[26] and Fe-contributing lithology within each catchment calculated as the sum of area from geologic mapping[24] of four Devonian-age *units (DOtu*, DOtp*, DOtm*, MDe*) that were associated with 78% of acid seeps, plus Quaternary surficial deposits (Qs) representing wetland-associated deposits. Area of geology and means of permafrost probability were calculated for each watershed in the statistical language R[74] using packages *tidyverse*[75], *raster*[76], *terra*[77], *sp*[78,79], and *sf*[80,81].

Our hypothesis testing defined the response variable $Y = \log_{10}$(dissolved Fe) and predictor variables: X_1= within-tributary catchment mean probability of near-surface (<1 m) permafrost[26] (*Near-surface permafrost probability*); X_2 = log-transformation of within-catchment area of the four mapped[24] Devonian-age*units (DOtu*, DOtp*, DOtm*, MDe*) associated with 78% of acid seeps plus the within-catchment area Qs (*Reactive geology area*); and $X_3 = X_1\ X_2$ as *Expected reactive geologic area exposed to near-surface permafrost*.

We compared four candidate models with the response variable Y = $\log_{10}$(dissolved Fe) with $\varepsilon \sim N(0,\sigma)$ representing error distributed normally with mean zero and standard deviation σ.

1. *Near-surface permafrost probability*-only: $Y = \beta_o + \beta_1 X_1 + \varepsilon$.
2. *Reactive geology area*-only $Y = \beta_o + \beta_2 X_2 + \varepsilon$.
3. *Expected reactive geologic area exposed to near-surface permafrost*: $Y = \beta_o + \beta_3 X_3 + \varepsilon$.
4. Two-variable permafrost and geology: $Y = \beta_o + \beta_1 X_1 + \beta_2 X_2 + \varepsilon$.

Model selection used adjusted-R^2 to account for model complexity and is reported in the main text as the percentage of variability in dissolved Fe explained by each model. Statistical significance (0.05) of coefficients was assessed using standard *t*-tests with $\alpha = 0.05$. To test whether Quaternary surficial deposits (Qs) contributed measurably to dissolved Fe, we built an alternative model excluding Qs from X_2 (creating X_2* containing only the four *units) and compared model fit. We applied the same approach to model sulfate concentrations, replacing Y with $\log_{10}(SO_4^{2-})$.

Iron flux estimation

To estimate mean iron fluxes in dissolved, total, and suspended particulate forms over each of two 27-day periods (30 June–26 July and 19 July–14 August 2023), we multiplied mean discharge over both periods by the point sample value of [Fe] in its dissolved, total, and particulate forms. Because none of the Salmon River's reaches or tributaries are gaged, we modeled discharge using a gridded (1 km) daily precipitation (mm/day) product known as Daymet[82] and USGS streamgage discharge[73] from ten northern Alaska locations (Supplementary Table 3) during the two 27-day periods in 2023 and a third in 2022 (27 July–22 August, 2022) for further validation of the discharge modeling approach.

Discharge modeling using Daymet: Our approach was to develop one model for each of the three periods to estimate discharge given modeled rainfall over a basin area. To construct the model, we extracted daily discharge data for each period using the R package *dataRetrieval*[83] from 10 USGS streamgages[73] (Fig. 2a) representing 10 different basins located among three regions defined by their ocean sea catchment (Supplementary Table 3). Among the 10 USGS streamgages, daily discharges varied 3.5–1838 m^3s^{-1} and basin areas ranged 28–35,882 km^2.

Daymet values were extracted from watershed boundaries in R with functions in *raster*[76], *terra*[77], *sp*[78,79], and *sf*[80,81]. In essence, we doubly integrated Daymet over each watershed area *A* and each period *D*. The integral value for each period at each of the $n = 10$ Arctic Alaska rivers with USGS streamgages provided the dependent variable ($\log_{10}$-transformed gage discharge) in a linear model that was regressed on Daymet integral value ($\log_{10}$-transformed values of the mean-daily Daymet precipitation within each watershed above the streamgage). We calculated *A* from a 5-m resolution interferometric synthetic aperture radar (IFSAR[84]) digital elevation model (DEM) downloaded from the Elevation Portal of the Alaska Division of Geological and Geophysical Surveys[85]. Applying hydrological tools in the R package *whitebox*[86,87] to the DEM with streamgage location as the lowest point on a watershed's boundary where water flows out of a catchment

(pour point) allowed us to delineate the catchment upstream of each pour point as a spatial polygon. Next, we extracted all Daymet pixels within the polygon for each day during a given sampling period, D, and summed them over the period and the watershed boundary, A. We calculated the double integral as "discharge from Daymet" and regressed log-transformed observed mean discharge from streamgages against log-transformed Daymet-derived discharge using simple linear regression. This provided two models (one for each sampling period in 2023) that we then applied to Daymet-derived discharge calculated at Fe sample locations on the Salmon River and at its tributaries that we treated as hydrological pour points.

Discharge models Modeled discharge approximated well the observed streamgage discharge (Supplementary Fig. 14). For the 30 June–26 July 2023 period, discharge = 0.91 Daymet$^{1.10}$, with $R^2 = 0.98$. For the 19 July–14 August 2023, discharge = 1.17 Daymet$^{0.98}$, with $R^2 = 0.95$. For 27 July–22 August 2022, discharge = 1.04 Daymet$^{0.93}$, with $R^2 = 0.97$. In each equation, discharge is in units of m^3s^{-1} and Daymet represents daily precipitation in the watershed as pixel values multiplied by pixel area summed over watershed and scaled to a daily average.

Local study area: Ikalukrok Creek near Red Dog Mine

RDM, 130 km N of Kotzebue (68.0675, -162.8472, 218-300 m asl, Fig. 2a) extracts lead-zinc sulfide ore and trucks the concentrate on an 80-km gravel road to a Chukchi Sea port. Following deposit discovery in the 1950s, drilling-based exploration began in 1980, road, port-site, and mine construction in 1987, and mining in 1989. Teck Alaska Incorporated (Teck; Anchorage, Alaska), provided year-round daily air temperature and precipitation from Bons Creek Wx (68.0291, -162.9118, 296 m asl) near the mine for use in modeling ground temperature using the GIPL2[29] model of the Geophysical Institute Permafrost Laboratory.

Ikalukrok Creek watershed seep pH, sulfate, and metals

The mine's operating company, Teck, its predecessor Cominco, and the State of Alaska have undertaken or contracted water quality and aquatic biota studies in nearby undisturbed catchments as controls on mining-effects since 1982[51–58]. Water quality monitoring expanded in 2011 following increases in naturally occurring ARD along Ikalukrok Creek above the Red Dog Creek confluence[55], and across a 200 km² area upstream, W, and N of the mine and its infrastructure. Here we rely on measurements of pH and TDS from a single water quality station on Ikalukrok Creek (Station 207) together with six other stations (Fig. 5a) sampled with a YSI ProDSS multi-parameter meter once per month during May–October. In September 2020, Teck also sampled eight acid seeps (Fig. 5a) for pH, sulfate, metals, and TDS.

In 2020, Teck contracted Kuna Engineering to determine SO_4^{2-} and metal concentrations at 18 seep locations. We selected the eight seep locations along upper Ikalukrok Creek above monitoring station Ikalukrok 207 for analysis (Fig. 5a). Using helicopter support over the course of 2 days, samples for total solids were collected directly into appropriately preserved bottles (i.e., acidified with 1% nitric acid for metals), while dissolved solid samples were collected in unpreserved containers and transported same-day-collected to Red Dog, where they were filtered (0.45 μm) into acidified containers.

Ikalukrok Creek stained tributary counts

We used Esri Wayback[66] and Google Earth Pro[65] imagery as well as eight 2017–2022 Planet Lab[64] scenes (3 m resolution) upstream of N 68.0940, W 162.9485 to investigate inter- and intra-annual variability in Ikalukrok Creek staining. Using staining visible on oblique aerial photography collected[56] 14 October 2019 to inform reflectance banding (NIR – red – blue), we located Ikalukrok tributary staining on satellite imagery and counted the number of stained tributaries. For each year with available imagery, we recorded the count of visibly stained tributaries during the July–October period when staining was most apparent. This metric was used to assess temporal relationships between ALT and visible rusting.

Ground temperature modeling and active layer thickness

Responding to widespread natural ARD (i.e., non-mine related) in 2018, Teck drilled four boreholes along a 220 m transect (Fig. 5a, 377–394 m asl) in an upper catchment of Ikalukrok Creek, 11.2 km NW and 100 m above the mine's roads and infrastructure. Two boreholes (Shrub BH1 and BH2) penetrated beneath shrub tundra of deciduous taxa <0.5 m tall (*Salix* spp., ericaceous shrubs, *Betula nana*). Two others penetrated beneath sedge tundra (*Carex* spp., *Eriophorum* spp.). Thermistor-based ground temperatures (TGT) were recorded in each borehole at 6–9 node depths (0.09–6.10 m below ground) during 3–5 years (2018–2023). Approximately 6.1 km distant, pH and TDS were measured instream several times each year (2015–2020) at Ikalukrok Creek Station 207 (Ikalukrok 207). TDS was also measured at six other stations in the Ikalukrok Creek watershed upstream of RDM (Fig. 5a).

We calculated modeled ground temperatures (MGT) 5.1 km upstream from Station 207 to identify and hindcast ALT using the ground temperature model GIPL2[29] with borehole TGT as calibration and Bons Creek air temperature and snow depth time series as upper boundary conditions. GIPL2 simulates heat flow over time and depth using an implicit finite difference method to numerically solve the one-dimensional heat conduction equation. Soil properties based on field description from drill logs and vegetation cover (Supplementary Table 2) parametrized the model, conditional on TGT and boundary conditions. GIPL2 accounts for thermal conductivity and heat capacity of soils, as well as unfrozen water and its latent heat of fusion during phase changes, improving accuracy of permafrost dynamics. The model includes time-varying snowpack depth, thermal conductivity, and heat capacity. To calculate snowpack depth, we divided Bons Creek Wx accumulated precipitation by an average snow density (0.3 g cm^{-3}) that is approximately equal to that reported as snow density[88] of North American tundra (0.28 g cm^{-3}). Snowpack thermal conductivity and other characteristics varied by borehole (Supplementary Table 2). Locations were: Sedge Tundra BH3 N 68.1829, W162.959582; Sedge Tundra BH4 N 68.182244, W162.957916; Shrub Tundra BH1 N 68.18178, W 162.95812; Shrub Tundra BH2 N 68.181434, W162.956096, all located within 47–212 m from one another at 377–394 m asl.

Initial soil thermal parameter values were selected from published ranges[89,90] and from drill log stratigraphy observations (Supplementary Table 2). The model ran 2010–2023. Model initialization began 8 years prior to measured TGT to reach a steady state for the 2018–2020 calibration period. The depth varying MGT values were compared to corresponding TGT values, then soil porosity, thermal conductivities for the thawed and frozen soil were systematically adjusted within plausible ranges to minimize error defined as $|TGT-MGT|$. Model calibration in the shrub tundra was improved by replacing Bons Creek Wx snowpack depth, S_d, as a boundary condition with 2.5 S_d to account for the additional snow accumulation in the shrub tundra. Sedge tundra required no adjustment to S_d for calibration.

Active layer thickness: The output of GIPL2 is a matrix of MGT values where each row is a depth and each column is a day. To estimate ALT, we classified each element of the matrix as above freezing or not to create a binary matrix. The active layer bottom on any given day was maximum depth where MGT >0 °C and the active layer top was calculated as the shallowest depth where MGT >0 °C. If no depths were unfrozen on a given date, both top and bottom were set to NA.

Error estimation: We estimated errors in mean daily ground temperature near the base of the active layer using values of TGT recorded at 6–9 node depths (0.09–6.10 m below ground) during 3–5 years (2018–2023). Supplementary Fig. 15 compares MGT and TGT at the depths where thermistors recorded ground temperature near the active layer depths. We also compared the measured ALT based on TGT > 0 (ALT_{obs}) to modeled thickness (ALT_{mod}) for the years of thermistor recording (Supplementary Figs. 16-19):

BH1 shrub tundra: model was well constrained (ALT_{mod} - ALT_{obs} = 0.33 m).

ALT_{obs} = 4.57 m <ALT_{mod} = 4.9 m < 6.1 m = next deepest thermistor

BH2 shrub tundra: the model missed the talik at 6.1 m from autumn 2021-spring 2023.

$4.8 \leq ALT_{mod} \leq 5.2$ m < 6.1 m = ALT_{obs} = 6.1 m = deepest thermistor

BH3 sedge tundra: model was well constrained (ALT_{mod} - ALT_{obs} = 0.47 m).

ALT_{obs} = 2.13 m <ALT_{mod} = 2.6 m < 2.74 m = next deepest thermistor

BH4 sedge tundra: model was well constrained (ALT_{mod} - ALT_{obs} = 0.48 m).

ALT_{obs} = 0.9 m <ALT_{mod} = 1.38 m < 1.52 m = next deepest thermistor

One-year lag analysis

To test for temporal relationships between permafrost thaw and stream ARD products, we compared 2014–2021 ALT from the four boreholes in the headwaters of West Fork Ikalukrok Creek at year T with 2015–2022 TDS measurements at year T + 1 for seven monitoring stations in the Iklaukrok Creek watershed located within 15 km of the boreholes and upstream of RDM effluent into Red Dog Creek (Fig. 5a). We calculated mean ALT across the four boreholes for each year T. TDS measurements were collected May–October for each year during 2015-2022 at each of seven monitoring stations (Fig. 5a): Ikalukrok 205, West Fork Ikalukrok Creek 206, Ikalukrok 207 (downstream of confluence with West Fork Ikalukrok Creek), East Fork Ikalukrok Creek 208, Station 9 (located on Ikalukrok Creek downstream of confluence with East Fork Ikalukrok Creek), Station 12 (located on Red Dog Creek upstream of confluence with RDM effluent) and Rachel Creek (a tributary of Red Dog Creek upstream of RDM).

To estimate the strength of relationships between TDS in year T + 1 and ALT in year T, we calculated R^2 for the regression of log-transformed each month's (May–October) TDS of year T + 1 on log-transformed mean ALT of year T at each of the seven monitoring stations. In addition, we calculated the Pearson's correlation coefficient between 2014 and 2022 ALT from the four boreholes in year T with 2015–2023 mean autumn (August–October, the period of maximum ALT and baseflow conditions) pH measured at the monitoring station Ikalukrok 207 in year T + 1. Statistical significance was assessed using standard Wald *t*-tests with $\alpha = 0.05$. To evaluate whether the temporal lag extended to visible stream staining, we correlated stained tributary counts (from satellite imagery analysis) in year Y + 1 with mean ALT from year Y. We also correlated stained tributary counts with contemporary TDS to confirm that visible staining reflects ARD chemical intensity.

Data availability

The chemical, sample location, and other data that support the findings of this study, including the source files for figures, are available at Figshare DOI 10.6084/m9.figshare.28091102.

Received: 17 January 2025; Accepted: 17 March 2026;
Published online: 06 April 2026

References

1. Ripple, W. J. et al. The 2024 state of the climate report: perilous times on planet Earth. *BioScience* **74**, 812–824 (2024).
2. Lacelle, D., Doucet, A., Clark, I. D. & Lauriol, B. Acid drainage generation and seasonal recycling in disturbed permafrost near Eagle Plains, northern Yukon Territory, Canada. *Chem. Geol.* **243**, 157–177 (2007).
3. Barker, A. J. et al. Iron oxidation–reduction processes in warming permafrost soils and surface waters expose a seasonally rusting Arctic watershed. *ACS Earth Space Chem* **7**, 1479–1495 (2023).
4. O'Donnell, J. A. et al. Metal mobilization from thawing permafrost to aquatic ecosystems is driving rusting of Arctic streams. *Commun. Earth Environ.* **5**, 268 (2024).
5. Sullivan, P. F. et al. Wild, scenic, and toxic: recent degradation of an iconic Arctic watershed with permafrost thaw. *Proc. Natl Acad. Sci. USA* **122**, e2425644122 (2025).
6. Todd, A. S. et al. Climate-change-driven deterioration of water quality in a mineralized watershed. *Environ. Sci. Technol.* **46**, 9324–9332 (2012).
7. Manning, A. H., Petach, T. N., Runkel, R. L. & McKnight, D. M. Climate-driven increases in stream metal concentrations in mineralized watersheds throughout the Colorado Rocky Mountains, USA. *Water Resour. Res.* **60**, 2023WR036062 (2024).
8. Zarroca, M., Roqué, C., Linares, R., Salminci, J. G. & Gutiérrez, F. Natural acid rock drainage in alpine catchments: a side effect of climate warming. *Sci. Total Environ.* **778**, 146070 (2021).
9. Santofimia, E., López-Pamo, E., Palomino, E. J., González-Toril, E. & Aguilera, Á Acid rock drainage in Nevado Pastoruri glacier area (Huascarán National Park, Perú): hydrochemical and mineralogical characterization and associated environmental implications. *Environ. Sci. Pollut. Res.* **24**, 25243–25259 (2017).
10. Walsh, E. V., Hilton, R. G., Tank, S. E. & Amos, E. Temperature sensitivity of the mineral permafrost feedback at the continental scale. *Sci. Adv.* **10**, 4893 (2024).
11. Jacobs, J. A., Lehr, J. H. & Testa, S. M. *Acid Mine Drainage, Rock Drainage, and Acid Sulfate Soils: Causes, Assessment, Prediction, Prevention, and Remediation* (John Wiley & Sons, 2014).
12. Lovley, D. R. Dissimilatory Fe(III) and Mn(IV) reduction. *Microbiol. Rev.* **55**, 259–287 (1991).
13. Weber, K. A., Achenbach, L. A. & Coates, J. D. Microorganisms pumping iron: anaerobic microbial iron oxidation and reduction. *Nat. Rev. Microbiol.* **4**, 752–764 (2006).
14. Herndon, E. et al. Influence of iron redox cycling on organo-mineral associations in Arctic tundra soil. *Geochim. Cosmochim. Acta* **207**, 210–231 (2017).
15. Herndon, E. et al. Iron and iron-bound phosphate accumulate in surface soils of ice-wedge polygons in arctic tundra. *Environ. Sci. Process. Impacts* **22**, 1475–1490 (2020).
16. Patzner, M. S. et al. Iron mineral dissolution releases iron and associated organic carbon during permafrost thaw. *Nat. Commun.* **11**, 6329 (2020).
17. Patzner, M. S. et al. Seasonal fluctuations in iron cycling in thawing permafrost peatlands. *Environ. Sci. Technol.* **56**, 4620–4631 (2022).
18. Callegary, J. B., Kikuchi, C. P., Koch, J. C., Lilly, M. R. & Leake, S. A. Groundwater in Alaska (USA). *Hydrogeol. J.* **21**, 25 (2013).
19. Brown, C. L. & Godduhn, A. Socioeconomic effects of declining salmon runs on the Yukon River. *Division of Subsistence Technical Paper*, 1–170 (Alaska Department of Fish and Game, 2015).
20. Kemeny, P. C. et al. Arctic permafrost thawing enhances sulfide oxidation. *Glob. Biogeochem. Cycles* **37**, 2022GB007644 (2023).
21. Jallen, D. M. et al. Yukon River salmon stock status and salmon fisheries, 2022: a report to the Alaska Board of Fisheries, January 2023. Alaska Department of Fish and Game Special Publication No. 22-20 (ADF&G, 2022).
22. Jorgenson, M. et al. Permafrost characteristics of Alaska. In *Proc. Ninth International Conference on Permafrost* 3, 121–122 (Institute of Northern Engineering, University of Alaska Fairbanks, 2008)
23. United States Geological Survey (USGS). *National Mineral Resource Assessment 1998: Circular 1178* (U.S. Geological Survey, 2001). https://doi.org/10.3133/cir1178.
24. Wilson, F. H., Hults, C. P., Mull, C. G. & Karl, S. M. *Geologic Map of Alaska*. U.S. Geological Survey Scientific Investigations Map 3340, pamphlet 196 p., 2 sheets, scale 1:1,584,000 (2015). https://doi.org/10.3133/sim3340.
25. Obu, J. et al. Northern Hemisphere permafrost map based on TTOP modelling for 2000–2016 at 1 km² scale. *Earth-Sci. Rev.* **193**, 299–316 (2019).
26. Pastick, N. J. et al. Distribution of near-surface permafrost in Alaska: estimates of present and future conditions. *Remote Sens. Environ.* **168**, 301–315 (2015).

27. Clawson, C. M. *Aquatic Biomonitoring at Red Dog Mine, 2022*. Alaska Department of Fish and Game, Technical Report No. 23-02 (Alaska Department of Fish and Game, Habitat Section, 2023).
28. Farquharson, L. M., Romanovsky, V. E., Kholodov, A. & Nicolsky, D. Sub-aerial talik formation observed across the discontinuous permafrost zone of Alaska. *Nat. Geosci.* **15**, 475–481 (2022).
29. Marchenko, S., Romanovsky, V. & Tipenko, G. Numerical modeling of spatial permafrost dynamics in Alaska. In *Proc. Ninth International Conference on Permafrost* Vol. 29, 1125–1130. (Institute of Northern Engineering, University of Alaska Fairbanks, 2008).
30. Tank, S. E. et al. Recent trends in the chemistry of major northern rivers signal widespread Arctic change. *Nat. Geosci.* **16**, 789–796 (2023).
31. Toohey, R. C., Herman-Mercer, N. M., Schuster, P. F., Mutter, E. A. & Koch, J. C. Multidecadal increases in the Yukon River Basin of chemical fluxes as indicators of changing flowpaths, groundwater, and permafrost. *Geophys. Res. Lett.* **43**, 12–120 (2016).
32. Zolkos, S., Tank, S. E. & Kokelj, S. V. Mineral weathering and the permafrost carbon–climate feedback. *Geophys. Res. Lett.* **45**, 9623–9632 (2018).
33. Calmels, D., Gaillardet, J., Brenot, A. & France-Lanord, C. Sustained sulfide oxidation by physical erosion processes in the Mackenzie River basin: climatic perspectives. *Geology* **35**, 1003–1006 (2007).
34. Burke, A. et al. Sulfur isotopes in rivers: insights into global weathering budgets, pyrite oxidation, and the modern sulfur cycle. *Earth Planet. Sci. Lett.* **496**, 168–177 (2018).
35. Colombo, N. et al. Permafrost thaw affects the chemistry of mountain ponds. *Environ. Res. Lett.* **20**, 094007 (2025).
36. Koch, J. C. et al. The dominance and growth of shallow groundwater resources in continuous permafrost environments. *Proc. Natl. Acad. Sci. USA* **121**, e2317873121 (2024).
37. Dial, R. J. et al. Arctic sea ice retreat fuels boreal forest advance. *Science* **383**, 877–884 (2024).
38. Morel, F. M. & Price, N. M. The biogeochemical cycles of trace metals in the oceans. *Science* **300**, 944–947 (2003).
39. Lipson, D. A., Jha, M., Raab, T. K. & Oechel, W. C. Reduction of iron(III) and humic substances plays a major role in anaerobic respiration in an Arctic peat soil. *J. Geophys. Res. Biogeosci.* **115**, G4 (2010).
40. Herndon, E. M. et al. Iron (oxyhydr)oxides serve as phosphate traps in tundra and boreal peat soils. *J. Geophys. Res. Biogeosci.* **124**, 227–246 (2019).
41. Brown, R. J., von Finster, A., Henszey, R. J. & Eiler, J. H. Catalog of Chinook salmon spawning areas in Yukon River basin in Canada and United States. *J. Fish Wildl. Manag.* **8**, 558–586 (2017).
42. Orth, D. J. *Dictionary of Alaska Place Names* No. 567 (US Government Printing Office, 1967).
43. Darby, D. A. & Bischof, J. F. A Holocene record of changing Arctic Ocean ice drift analogous to the effects of the Arctic Oscillation. *Paleoceanography* **19**, PA1027 (2004).
44. Alaska ShoreZone. *Arctic Impressions: A Photographic Journey Along Alaska's Arctic Coast* (National Oceanic and Atmospheric Administration, 2014). https://repository.library.noaa.gov/view/noaa/17387.
45. Craig, P. C. & McCart, P. J. Classification of stream types in Beaufort Sea drainages between Prudhoe Bay, Alaska, and the Mackenzie delta, NWT, Canada. *Arct. Alp. Res.* **7**, 183–198 (1975).
46. Gallant, A. L., Binnian, E. F., Omernik, J. M. & Shasby, M. B. Ecoregions of Alaska. *U.S. Geological Survey Professional Paper* **1567** (U.S. Government Printing Office, 1995).
47. Kaufman, D. S., Young, N. E., Briner, J. P. & Manley, W. F. Alaska palaeo-glacier atlas (version 2). *Dev. Quat. Sci.* **15**, 427–445 (2011).
48. Geck, J., Hock, R. & Nolan, M. Geodetic mass balance of glaciers in the Central Brooks Range, Alaska, USA, from 1970 to 2001. *Arct. Antarct. Alp. Res.* **45**, 29–38 (2013).
49. Jorgenson, M. T. et al. *An Ecological Land Survey and Landcover Map of the Arctic Network. Natural Resource Technical Report NPS/ARCN/NRTR-2009/270* (National Park Service, 2009).
50. Moore, D. W., Young, L. E., Modene, J. S. & Plahuta, J. T. Geologic setting and genesis of the Red Dog zinc-lead-silver deposit, western Brooks Range, Alaska. *Econ. Geol.* **81**, 1696–1727 (1986).
51. Weber Scannell, P. & Ott, A. G. *Fisheries Resources and Water Quality, Red Dog Mine. Alaska Department of Fish and Game, Technical Report* (Alaska Department of Fish and Game, Habitat and Restoration Division, 1998).
52. Weber Scannell, P., Ott, A. G. & Morris, W. A. *Fish and Aquatic Taxa Report, Red Dog Mine (1998–1999). Technical Report No. 00-3* (Alaska Department of Natural Resources, Division of Habitat and Restoration, 2000).
53. Ott, A. G. & Morris, W. A. *Aquatic Biomonitoring at Red Dog Mine, 2006. NPDES Permit No. AK-003865-2, Technical Report No. 07-03* (Alaska Department of Natural Resources, Office of Habitat Management and Permitting, 2007).
54. Ott, A. G. & Morris, W. A. *Aquatic Biomonitoring at Red Dog Mine, 2007. NPDES Permit No. AK-003865-2, Technical Report No. 08-02* (Alaska Department of Natural Resources, Office of Habitat Management and Permitting, 2008).
55. Ott, A. G. & Morris, W. A. *Aquatic Biomonitoring at Red Dog Mine, 2014. APDES Permit No. AK-0038652 (Modification #1), Technical Report No. 15-01* (Alaska Department of Fish and Game, Division of Habitat, 2015).
56. Bear, C. *Ikalukrok Creek near Red Dog Mine. Trip Report* (Alaska Department of Fish and Game, Habitat Section, 2019).
57. Clawson, C. M. & Ott, A. G. *Aquatic Biomonitoring at Red Dog Mine, 2020. APDES Permit No. AK0038652 (Modification #1), Technical Report No. 21-04* (Alaska Department of Fish and Game, Habitat Section, 2021).
58. Clawson, C. M. *Aquatic Biomonitoring at Red Dog Mine, 2023. Technical Report No. 24-04* (Alaska Department of Fish and Game, Habitat Section, 2024).
59. National Oceanic and Atmospheric Administration (NOAA) National Centers for Environmental Information (NCEI). Daily Summaries, Station: Kotzebue Airport, AK US (GHCND:USW00026616). Climate Data Online (accessed 9 February 2026). https://www.ncdc.noaa.gov/cdo-web/datasets/GHCND/stations/GHCND:USW00026616/detail.
60. Hill, K. H. & Sousanes, P. J. National Park Service Arctic Inventory and Monitoring Network Quality Controlled Climate Dataset (accessed 9 February 2026). https://irma.nps.gov/DataStore/Reference/Profile/2239061.
61. Mahoney, A. R. et al. Thin ice, deep snow and surface flooding in Kotzebue Sound: landfast ice mass balance during two anomalously warm winters and implications for marine mammals and subsistence hunting. *J. Glaciol.* **67**, 1013–1027 (2021).
62. Maxar Technologies. IKONOS, GeoEye, and WorldView Satellite Imagery. https://www.maxar.com (accessed 9 February 2026).
63. Copernicus Sentinel-2 Data. European Space Agency (ESA). https://dataspace.copernicus.eu (accessed 9 February 2026).
64. Team, Planet *Planet Application Program Interface: In Space for Life on Earth (Planet Labs PBC)* https://www.planet.com (accessed 9 February 2026).
65. Google. Google Earth Pro. https://www.google.com/earth/ (accessed 9 February 2026).
66. Esri. Wayback—World Imagery. https://livingatlas.arcgis.com/wayback/ (accessed 9 February 2026).
67. European Space Agency. Copernicus Browser. https://browser.dataspace.copernicus.eu (accessed 9 February 2026).
68. Kelley, K. D. & Taylor, C. D. Natural environmental effects associated with the Drenchwater zinc-lead-silver massive sulfide deposit with comparisons to the Red Dog and Lik deposits, west-central Brooks Range, Alaska. In *Geologic Studies in Alaska by the US Geological Survey During 1994 (US Geological Survey Bulletin 2152)* (eds Moore, T. E. & DeMoulin, J. A.) 31–45 (US Geological Survey, 1996).

69. Leach, D. L. et al. Nature of hydrothermal fluids at the shale-hosted Red Dog Zn-Pb-Ag deposits, Brooks Range, Alaska. *Econ. Geol.* **99**, 1449–1480 (2004).
70. Reynolds, M. A. et al. Diagenetic controls on the formation of the Anarraaq clastic-dominated Zn-Pb-Ag deposit, Red Dog district, Alaska. *Econ. Geol.* **116**, 1803–1824 (2021).
71. Hitzman, M. W., Proffett, J. M., Schmidt, J. M. & Smith, T. E. Geology and mineralization of the Ambler district, northwestern Alaska. *Econ. Geol.* **81**, 1592–1618 (1986).
72. Folger, P. F. & Schmidt, J. M. Geology of the carbonate-hosted Omar copper prospect, Baird Mountains, Alaska. *Econ. Geol.* **81**, 1690–1695 (1986).
73. U.S. Geological Survey. USGS water data for the Nation: U.S. Geological Survey National Water Information System database (accessed 9 February 2026). https://doi.org/10.5066/F7P55KJN (2026).
74. R Core Team. *R: A Language and Environment for Statistical Computing v.4.4.1* (R Foundation for Statistical Computing, 2024); https://www.R-project.org/.
75. Wickham, H. et al. Welcome to the tidyverse. *J. Open Source Softw.* **4**, 1686 (2019).
76. Hijmans, R. J. *raster: Geographic Data Analysis and Modeling. R package version 3.6-26* (2023); https://CRAN.R-project.org/package=raster.
77. Hijmans, R. J. terra: Spatial Data Analysis. R package version 1.7-78 (2024); https://CRAN.R-project.org/package=terra.
78. Pebesma, E. J. & Bivand, R. S. Classes and methods for spatial data in. *R. R News* **5**, 9–13 (2005).
79. Bivand, R. S., Pebesma, E. & Gomez-Rubio, V. *Applied Spatial Data Analysis with R* 2nd edn (Springer, 2013).
80. Pebesma, E. Simple features for R: standardized support for spatial vector data. *R J.* **10**, 439–446 (2018).
81. Pebesma, E. & Bivand, R. *Spatial Data Science: With Applications in R* (Chapman and Hall/CRC, 2023). https://doi.org/10.1201/9780429459016
82. Thornton, M. M., Shrestha, R., Wei, Y., Thornton, P. E. & Kao, S.-C. *Daymet: Daily Surface Weather Data on a 1-km Grid for North America, Version 4 R1* (ORNL DAAC, 2022). https://doi.org/10.3334/ORNLDAAC/2129.
83. De Cicco, L. A., Hirsch, R. M., Lorenz, D., Watkins, W. D. & Johnson, M. *dataRetrieval: R Packages for Discovering and Retrieving Water Data Available from Federal Hydrologic Web Services, v.2.7.15* (2024). https://doi.org/10.5066/P9X4L3GE.
84. U.S. Geological Survey. *Digital Elevation—Interferometric Synthetic Aperture Radar (IFSAR)—Alaska* (USGS Earth Resources Observation and Science Center, 2013). https://doi.org/10.5066/P9C064CO.
85. *DGGS Staff. Elevation Datasets of Alaska. Alaska Division of Geological & Geophysical Surveys Digital Data Series 4* (2013). https://doi.org/10.14509/25239.
86. Lindsay, J. B. Whitebox GAT: a case study in geomorphometric analysis. *Comput. Geosci.* **95**, 75–84 (2016).
87. Wu, Q. & Brown, A. whitebox: 'WhiteboxTools' R Frontend. R package version 2.2.0 (2022); https://CRAN.R-project.org/package=whitebox.
88. Sturm, M. et al. Estimating snow water equivalent using snow depth data and climate classes. *J. Hydrometeorol.* **11**, 1380–1394 (2010).
89. Chen, S. et al. Soil thermal regime alteration under experimental warming in permafrost regions of the central Tibetan Plateau. *Geoderma* **372**, 114397 (2020).
90. Romanovsky, V. E. & Osterkamp, T. E. Effects of unfrozen water on heat and mass transport processes in the active layer and permafrost. *Permafr. Periglac. Process.* **11**, 219–239 (2000).

Acknowledgements

Funding for this work was provided by awards from the National Science Foundation to P.F.S. and R.J.D. (OPP-2325290) and to T.W.L. (OPP-2325291). R.J.D. also received support for this work from the Wilburforce Foundation and from NASA through the Alaska Space Grant Program (80NSSC20M0070). J. Cummings, E. Sieh, and Bering Air Service provided aviation support. A. Dahl, F. McCarthy, R. Kolesar, A. Lee, L. Adkins, and M. Zietlow provided valuable field assistance in the field. Tom Wetherell provided the location of the river rusting in Russia. Field sampling was permitted by the National Park Service (permit# KOVA-2023-SCI-0001). We acknowledge the donation of packrafts from Alpacka Raft, LLC and equipment from Hyperlight Mountain Gear that made data collection possible. Any use of trade, firm, or product names is for descriptive purposes only and does not imply endorsement by the U.S. Government.

Author contributions

R.J.D. conceived the study, led field data collection, performed data archiving and remote sensing interpretation, spatial and statistical analyzes, and wrote the manuscript. C.T.H. contributed to field data collection, data archiving, remote sensing interpretation, permafrost modeling by calibrating the GIPL2 ground temperature model, and manuscript preparation. P.F.S. contributed to study design, field data collection, aquatic ecosystem interpretation, and manuscript preparation. D.J.C. contributed to study design, contributed to field data collection, wetland ecosystem interpretation, and manuscript preparation. C.J.T. contributed to field data collection and manuscript preparation. D.D.G. contributed to field data collection, geological interpretation, and manuscript preparation. C.D. performed ICP-MS laboratory analyzes. M.R. provided water quality monitoring data from the Ikalukrok Creek watershed. D.J.N. developed and calibrated the GIPL2 ground temperature model and contributed to permafrost analysis and manuscript preparation. K.H. contributed climate data, remote sensing interpretation, and manuscript preparation. G.I. contributed to permafrost analysis and manuscript preparation. J.C.K. contributed to hydrological analysis and manuscript preparation. M.P.C. contributed to aquatic ecosystem interpretation and manuscript preparation. L.M. contributed to geological interpretation, regional context, and manuscript preparation. T.W.L. contributed to field data collection, geological and geochemical interpretation, laboratory supervision, and manuscript preparation. All authors reviewed and approved the final manuscript.

Competing interests

The authors declare the following competing interests: M.R. is employed by Teck Alaska Incorporated, which operates Red Dog Mine in the local study area and provided water quality monitoring data and borehole ground temperature data used in this study. L.M. is employed by NANA Regional Corporation, an Alaska Native regional corporation with land interests in the study area.

Additional information

Supplementary information The online version contains supplementary material available at https://doi.org/10.1038/s43247-026-03450-x.

Correspondence and requests for materials should be addressed to Roman J. Dial.

Peer review information Communications Earth and Environment thanks Catherine Hirst and the other, anonymous, reviewer(s) for their contribution to the peer review of this work. Primary Handling Editor: Alireza Bahadori. A peer review file is available.

Reprints and permissions information is available at http://www.nature.com/reprints

Publisher's note Springer Nature remains neutral with regard to jurisdictional claims in published maps and institutional affiliations.

Open Access This article is licensed under a Creative Commons Attribution-NonCommercial-NoDerivatives 4.0 International License, which permits any non-commercial use, sharing, distribution and reproduction in any medium or format, as long as you give appropriate credit to the original author(s) and the source, provide a link to the Creative Commons licence, and indicate if you modified the licensed material. You do not have permission under this licence to share adapted material derived from this article or parts of it. The images or other third party material in this article are included in the article's Creative Commons licence, unless indicated otherwise in a credit line to the material. If material is not included in the article's Creative Commons licence and your intended use is not permitted by statutory regulation or exceeds the permitted use, you will need to obtain permission directly from the copyright holder. To view a copy of this licence, visit http://creativecommons.org/licenses/by-nc-nd/4.0/.

© The Author(s) 2026